

DUDLEY KNOX LIBRARY
NAVAL POSTGRADUATE SCHOOL
MONTEREY CA 93943-5101

REPORT DOCUMENTATION PAGE

1a. REPORT SECURITY CLASSIFICATION UNCLASSIFIED			1b. RESTRICTIVE MARKINGS		
2a. SECURITY CLASSIFICATION AUTHORITY			3. DISTRIBUTION/AVAILABILITY OF REPORT Approved for public release; distribution is unlimited.		
2b. DECLASSIFICATION/DOWNGRADING SCHEDULE					
4. PERFORMING ORGANIZATION REPORT NUMBER(S)			5. MONITORING ORGANIZATION REPORT NUMBER(S)		
6a. NAME OF PERFORMING ORGANIZATION Naval Postgraduate School		6b. OFFICE SYMBOL (If applicable) 55	7a. NAME OF MONITORING ORGANIZATION Naval Postgraduate School		
6c. ADDRESS (City, State, and ZIP Code) Monterey, CA 93943-5000			7b. ADDRESS (City, State, and ZIP Code) Monterey, CA 93943-5000		
8a. NAME OF FUNDING/SPONSORING ORGANIZATION		8b. OFFICE SYMBOL (If applicable)	9. PROCUREMENT INSTRUMENT IDENTIFICATION NUMBER		
8c. ADDRESS (City, State, and ZIP Code)			10. SOURCE OF FUNDING NUMBERS		
			Program Element No.	Project No.	Task No.
					Work Unit Accession Number
11. TITLE (Include Security Classification) REAL-TIME DETECTION OF FATIGUE CRACKS AT MULTIPLE HOLES IN 7075 ALUMINUM USING ACOUSTIC EMISSION					
12. PERSONAL AUTHOR(S) FLATLEY, THOMAS					
13a. TYPE OF REPORT Master's Thesis		13b. TIME COVERED From To		14. DATE OF REPORT (year, month, day) September 1992	
				15. PAGE COUNT 76	
16. SUPPLEMENTARY NOTATION The views expressed in this thesis are those of the author and do not reflect the official policy or position of the Department of Defense or the U.S. Government.					
17. COSATI CODES			18. SUBJECT TERMS (continue on reverse if necessary and identify by block number)		
FIELD	GROUP	SUBGROUP			
			Acoustic emission, fatigue cracks		
19. ABSTRACT (continue on reverse if necessary and identify by block number)					
<p>In the E-2C Hawkeye's wing center section, stress fractures have been identified in the main beam web section. The cracks occurred in several web section attachment holes. Previous work, concerned with fatigue data, used a finite element code to design a specimen which modeled the actual section of the beam at one particular fastener hole near wing station 49. Acoustic emission testing was used to determine if crack initiation could be identified. In this work, acoustic emission techniques were applied to the monitoring of multiple cracks. The E-2C fatigue spectrum was used to load the specimens but fatigue testing was not an objective. Specimens were modified by drilling holes and attaching angles that represented the structural shapes used to attach the section to the wing skin. The original one-hole configuration and the new multiple hole specimen were tested. The cap angles were found to create a great deal of noise containing frequency components below 400kHz. Special high pass filters were fabricated which eliminated most of this noise. It was shown that linear location could be used to discriminate between crack growth signals and the filtered noise signals.</p>					
20. DISTRIBUTION/AVAILABILITY OF ABSTRACT <input checked="" type="checkbox"/> UNCLASSIFIED/UNLIMITED <input type="checkbox"/> SAME AS REPORT <input type="checkbox"/> DTIC USERS			21. ABSTRACT SECURITY CLASSIFICATION Unclassified		
22a. NAME OF RESPONSIBLE INDIVIDUAL GORMAN, M. R.			22b. TELEPHONE (Include Area code) (408) 646-2491		22c. OFFICE SYMBOL AA/Go

Approved for public release; distribution is unlimited.

REAL - TIME DETECTION OF FATIGUE CRACKS
AT MULTIPLE HOLES IN 7075 ALUMINUM USING ACOUSTIC EMISSION

by

Thomas Flatley
Lieutenant, United States Navy
B.S., Parks College of St. Louis University, 1984

Submitted in partial fulfillment
of the requirements for the degree of

MASTER OF SCIENCE IN AERONAUTICAL ENGINEERING

from the

NAVAL POSTGRADUATE SCHOOL
September, 1992

ABSTRACT

In the E-2C Hawkeye's wing center section, stress fractures have been identified in the main beam web section. The cracks occurred in several web section attachment holes. Previous work, concerned with fatigue data, used a finite element code to design a specimen which modeled the actual section of the beam at one particular fastener hole near wing station 49. Acoustic emission testing was used to determine if crack initiation could be identified. In this work, acoustic emission techniques were applied to the monitoring of multiple cracks. The E-2C fatigue spectrum was used to load the specimens but fatigue testing was not an objective. Specimens were modified by drilling holes and attaching angles that represented the structural shapes used to attach the section to the wing skin. The original one-hole configuration and the new multiple hole specimen configuration were tested. The cap angles were found to create a great deal of noise containing frequency components below 400kHz. Special high pass filters were fabricated which eliminated most of this noise. It was shown that linear location could be used to discriminate between crack growth signals and the filtered noise signals.

11000
F49677
C.1

TABLE OF CONTENTS

I.	INTRODUCTION	1
II.	WAVE THEORY.....	4
	A. FLEXURAL WAVE.....	4
	B. EXTENSIONAL WAVE.....	13
	C. LINEAR LOCATION.....	17
III.	INSTRUMENTATION.....	19
	A. EXPERIMENTAL SET-UP.....	19
	B. SPECIMEN MODIFICATION AND SPECTRUM LOADING.....	19
	C. MECHANICAL TESTING EQUIPMENT.....	24
	D. ACOUSTIC EMISSION INSTRUMENTATION.....	25
	1. Transducers.....	26
	2. Digital Storage Oscilloscope.....	28
	E. VIDEO MICROSCOPY.....	29
	F. FILTERING.....	30
IV.	RESULTS.....	33
	A. LEAD BREAK CALCULATIONS.....	33
	B. CRACK GROWTH AND SIGNAL LOCATION.....	37
V.	CONCLUSIONS.....	41
	APPENDIX A: FILTERS.....	43
	APPENDIX B: LEAD BREAKS.....	48
	APPENDIX C: CRACK/NOISE SIGNALS.....	53
	LIST OF REFERENCES.....	68
	INITIAL DISTRIBUTION LIST.....	70

I. INTRODUCTION

This thesis demonstrated the use of linear location of acoustical emission (AE) signals to detect multiple crack growth signals from multiple holes in a laboratory specimen (7075 Al). The waves produced by crack growth could be discriminated from extraneous noise signals by the extensional mode velocity. High pass filtering was used to eliminate much of the extraneous noise created by modifications to specimens based on a design from previous work by Smith [Ref. 1]. Smith fatigue tested an aluminum plate configured to simulate the stress conditions in the vicinity of wing station 49 in the wing center section of the E-2C Hawkeye and used acoustic emission techniques to detect crack initiation during testing. The objective of the current work was to demonstrate that acoustic emission monitoring techniques could detect crack signals in multiple holed specimens with cap angles changing the waveforms and creating more noise.

The Grumman E-2C is a fixed wing, carrier based, turboprop aircraft. Through the years, the aircraft's basic design has remained the same, though advancements in it's mission of airborne early warning demanded the most advanced avionics upgrades. In order to identify effects of increased weight due to the avionics and engine upgrades and to validate the expected useful life of 10,000 flight hours, fatigue testing of a full-scale airframe was conducted at Grumman's Bethpage plant [Ref. 2]. After 7,600 experimental flight hours, the fatigue test was stopped because of the observation of cracks in the wing center section [Ref. 3]. A 0.06" crack had developed in the main wing beam during testing, resulting from the combined stress concentration effects of a fuel transfer cutout and a nearby attachment hole used for securing the skin of the aircraft to the main beam. The

results of the Teardown Inspection Report identified this area as one of interest and in need of further study [Ref. 3].

Acoustic emission has evolved as a tool in non-destructive testing (NDT) but in its application to aircraft, it has been limited due to the large amount of extraneous noise created in a typical flight. Initial work in the field of stress wave characterization in 7075-T6 aluminum, which is used in the E-2C aircraft, was performed by Gerberich and Hartblower [Ref. 4]. They utilized a bandpass filter of 2-6 kHz to filter out low frequency machine noise during static testing and found that the crack growth rate was a linear function of the stress wave amplitude in 7075-T6 aluminum and other metals. McBride, Maclachlan and Paradis [Ref. 5] identified experimentally the fracture of intermetallic inclusions in 7075-T6 as the source of acoustic emission and showed that the maximum amplitude of a crack growth signal was approximately 10 times smaller than that of crack rubbing and fretting.

Harris and Dunegan [Ref. 6] classified cracking in 7075-T6 aluminum using rise time discrimination, defined as the time it takes for the amplified signal to reach its maximum voltage. Crack growth was noted as being associated with signals that rose quickly to peak amplitude as opposed to fretting and rubbing that had slow rise time events. Load cycle gating, 100-300 kHz bandpass filters centered on the resonant frequency of the transducers, and high gains of 60-80 dB for increased sensitivity were used.

Wadin and Dunegan [Ref. 7] expanded on techniques of spatial and bandpass filtering, developing a discrimination scheme based on the width of the received signal pulse, defined as the amount of time the signal remains above a preset threshold. They noted that the widths of crack growth signal pulses were shorter than the noise signals during fatiguing of 7075-T6 aluminum.

Bailey [Ref. 8] successfully monitored crack growth in 7075-T6 aluminum during low cycle fatigue using 500kHz high pass filtering of the signal. Later work on the fatigue of aluminum used the noise discrimination techniques of bandpass filtering, load cycle gating, spatial discrimination and damping of background and machine noises.

Recently, research in AE has shifted more to understanding the waveforms produced by crack growth so that noise discrimination can be accomplished more readily. The separation of the AE stress waves in aluminum thin plates into extensional and flexural components were shown by Gorman [Ref. 9]. Smith [Ref. 1] showed that AE events from crack growth under spectrum fatigue could be identified by the extensional mode and that the noise waveforms were easily separated due to the dissimilar shape and frequency content present.

II. WAVE THEORY

From Gorman [Ref. 9], it was discovered that in thin plates (wavelength is much greater than plate thickness) that only two wave modes were excited by the AE sources. These two modes are the extensional and flexural plate modes. In the following sections, governing equations and resulting dispersion relations for these two modes are derived and linear location used for the determination of the AE source is discussed.

A. FLEXURAL WAVE

The derivation of the equations of motion for a flexural wave in a thin plate considers an infinite plate of thickness, h , as in Figure II.1 [Ref. 10]. A differential element, $h \times dx \times dy$, is subjected to shear forces per unit length, Q , bending and twisting moments per unit length, M , and external loads per unit area, q . Only the force equation of motion in the z -direction and the two moment equations of motion about the x - and y -axis are considered. The other equations constitute the trivial case.

By neglecting rotary-inertia effects and higher order contributions from q to the moments, the resulting equations of motion are given as

$$-Q_x dy + (Q_x + \frac{\partial Q_x}{\partial x} dx) dy - Q_y dx + (Q_y + \frac{\partial Q_y}{\partial y} dy) dx + q dx dy = \rho h dx dy \frac{\partial^2 w}{\partial t^2}, \quad (1)$$

$$(M_y + \frac{\partial M_y}{\partial y} dy) dx - M_y dx + M_{xy} dy - (M_{xy} + \frac{\partial M_{xy}}{\partial x} dx) dy - Q dx dy = 0 \quad (2)$$

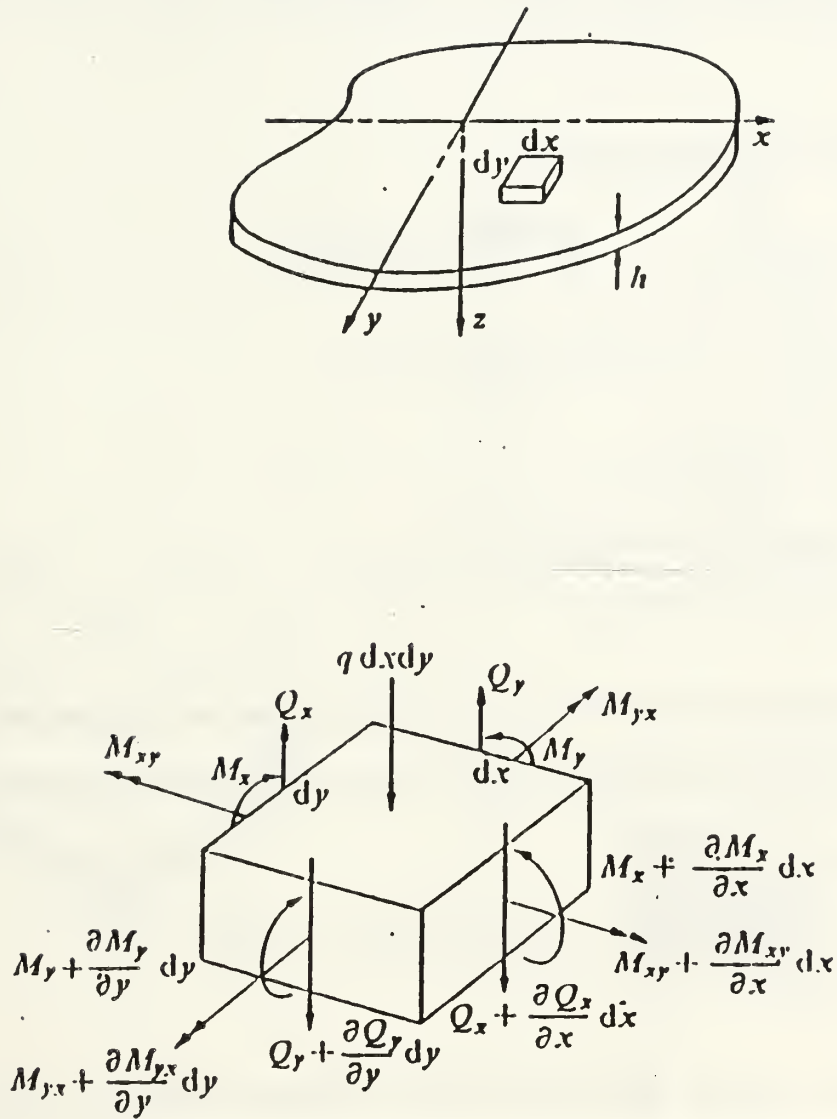


Figure II.1: Infinite Plate and Element Forces(after Graff [Ref. 10])

and

$$(M_y + \frac{\partial M_x}{\partial x} dx) dy - M_x dx + M_{xy} dy - (M_{yx} + \frac{\partial M_{yx}}{\partial y} dy) dx - M_{yx} dx - Q_x dy dx = 0. \quad (3)$$

Canceling like terms, these reduce to

$$\frac{\partial Q_x}{\partial x} + \frac{\partial Q_y}{\partial y} + q = \rho h \frac{\partial^2 w}{\partial t^2}, \quad (4)$$

$$\frac{\partial M_y}{\partial y} - \frac{\partial M_{xy}}{\partial x} - Q_y = 0 \quad (5)$$

and

$$\frac{\partial M_x}{\partial x} + \frac{\partial M_{yx}}{\partial y} - Q_x = 0. \quad (6)$$

Equations (5) and (6) are solved for Q_x and Q_y and substituted into equation (4).

From this, the following equation of motion in terms of moments is obtained

$$\frac{\partial^2 M_x}{\partial x^2} + \frac{\partial^2 M_{yx}}{\partial x \partial y} - \frac{\partial^2 M_{xy}}{\partial y \partial x} + \frac{\partial^2 M_y}{\partial y^2} + q = \rho h \frac{\partial^2 w}{\partial t^2}. \quad (7)$$

Kinematics of plate deformation and the differential element must now be considered and are illustrated in Figure II.2 [Ref. 10]. With the assumption that

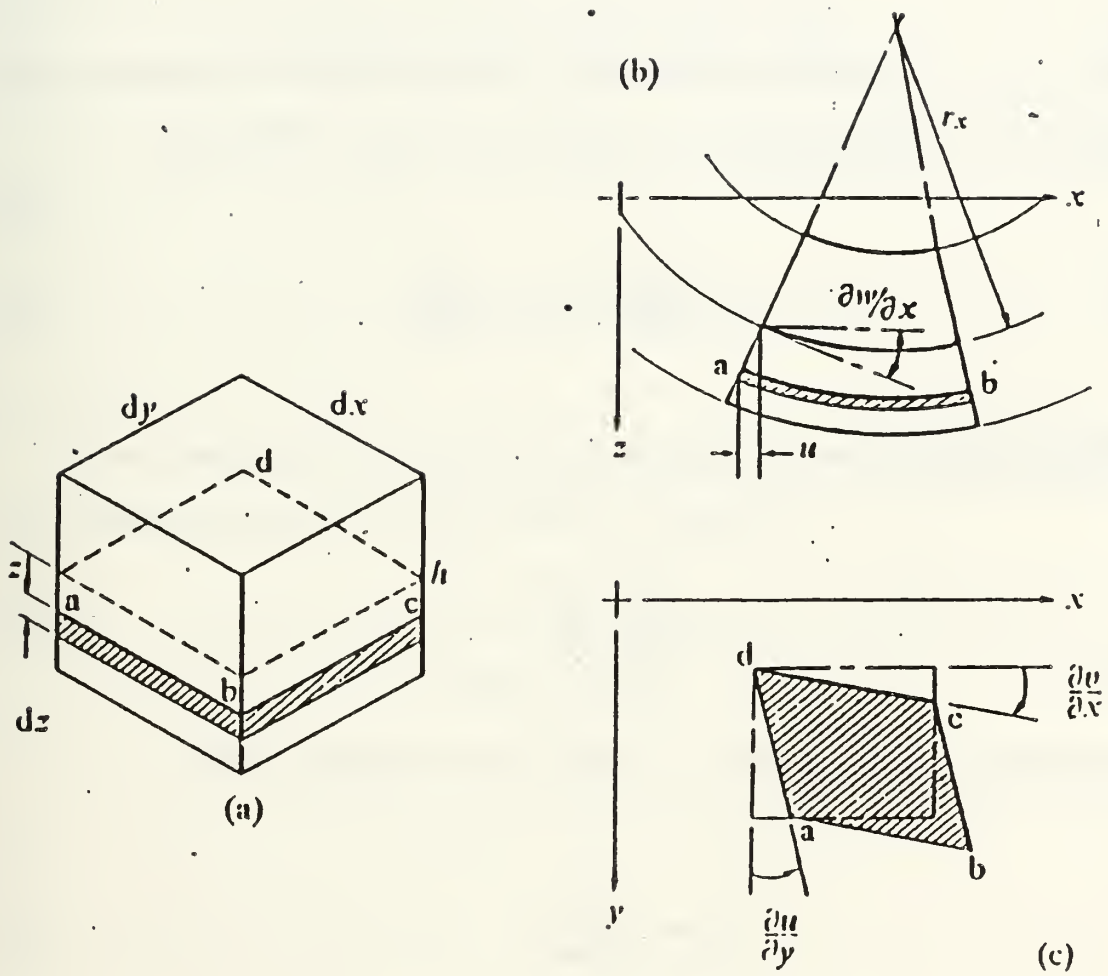


Figure II.2: Differential Plate Element (after Graff [Ref. 10])

plane sections remain plane and perpendicular to the mid-plane, the normal strains are given as

$$\epsilon_x = \frac{z}{r_x} \quad \text{and} \quad \epsilon_y = \frac{z}{r_y} \quad (8)$$

Here r_x and r_y define radii of curvature. For small slopes and deflections, the curvature may be approximated by $-\partial^2 w / \partial x^2$ and $-\partial^2 w / \partial y^2$. This yields

$$\epsilon_x = -z \frac{\partial^2 w}{\partial x^2} \quad \text{and} \quad \epsilon_y = -z \frac{\partial^2 w}{\partial y^2}. \quad (9)$$

The engineering shear strain is defined as

$$\gamma_{xy} = \frac{\partial u}{\partial y} + \frac{\partial v}{\partial x}. \quad (10)$$

Here displacements are given by $u = -z \partial w / \partial x$ and $v = -z \partial w / \partial y$, so that

$$\gamma_{xy} = -2z \frac{\partial^2 w}{\partial x \partial y}. \quad (11)$$

From Hooke's law the stresses are defined as

$$\sigma_x = \frac{E}{1-\nu^2}(\varepsilon_x + \nu\varepsilon_y) = -\frac{Ez}{1-\nu^2}\left(\frac{\partial^2 w}{\partial x^2} + \nu\frac{\partial^2 w}{\partial y^2}\right), \quad (12)$$

$$\sigma_y = \frac{E}{1-\nu^2}(\varepsilon_y + \nu\varepsilon_x) = -\frac{Ez}{1-\nu^2}\left(\frac{\partial^2 w}{\partial y^2} + \nu\frac{\partial^2 w}{\partial x^2}\right) \quad (13)$$

and

$$\tau_{xy} = G\gamma_{xy} = -2Gz\frac{\partial^2 w}{\partial x\partial y}. \quad (14)$$

These equations are then used to evaluate the bending and twisting moments.

The bending moment on face $h \times dy$ due to σ_x is given by

$$M_x dy = \int_{-h/2}^{h/2} z \sigma_x dy dx \quad (15)$$

or

$$M_x = \int_{-h/2}^{h/2} z \sigma_x dz. \quad (16)$$

By substituting the expression for σ_x in equation (12) into equation (16) and integrating, the following is obtained

$$M_x = -D\left(\frac{\partial^2 w}{\partial x^2} + \nu \frac{\partial^2 w}{\partial y^2}\right). \quad (17)$$

D, the flexural rigidity, is defined as

$$D = \frac{Eh^2}{12(1-\nu^2)}. \quad (18)$$

Similarly, for M_y

$$M_y = -D\left(\frac{\partial^2 w}{\partial y^2} + \nu \frac{\partial^2 w}{\partial x^2}\right). \quad (19)$$

The equation for M_{xy} is different, requiring a negative sign to compensate the positive shear stress for the sign convention established

$$M_{xy} = \int_{-h/2}^{h/2} z \tau_{xy} dz. \quad (20)$$

Integrating yields

$$M_{xy} = D(1-\nu^2) \frac{\partial^2 w}{\partial x \partial y}. \quad (21)$$

Since $M_{xy} = -M_{yx}$, the equation of motion (7) may now be written as

$$D\left(\frac{\partial^4 w}{\partial x^4} + 2\frac{\partial^4 w}{\partial^2 x \partial^2 y} + \frac{\partial^4 w}{\partial y^4}\right) - q = -\rho h \frac{\partial^2 w}{\partial t^2}. \quad (22)$$

Here the expression inside the parenthesis can be reduced to

$$\frac{\partial^4 w}{\partial x^4} + 2\frac{\partial^4 w}{\partial^2 x \partial^2 y} + \frac{\partial^4 w}{\partial y^4} = \left(\frac{\partial^2}{\partial x^2} + \frac{\partial^2}{\partial y^2}\right)\left(\frac{\partial^2 w}{\partial x^2} + \frac{\partial^2 w}{\partial y^2}\right) = \nabla^2 \nabla^2 w. \quad (23)$$

Thus, the governing equation for the flexural wave in a thin plate is given by

$$D\nabla^4 w(x, y, t) + \rho h \frac{\partial^2 w(x, y, t)}{\partial t^2} = q(x, y, t). \quad (24)$$

For a wave propagating in the plate, consider a solution as a harmonic wave of the form

$$w = Ae^{i(kr - \omega t)}. \quad (25)$$

This yields, for the various terms

$$\nabla^2 w = -Ak^2 e^{i(kr - \omega t)}, \quad (26)$$

$$\nabla^4 w = Ak^4 e^{i(kr - \omega t)} \quad (27)$$

and

$$\frac{\partial^2 w}{\partial t^2} = -A \omega^2 e^{i(kx - \omega t)}. \quad (28)$$

Because interest lies in wave propagation in an infinite medium with no immediate sources, $q=0$. Substituting into equation (24), the following is obtained

$$DAk^2 e^{i(kx - \omega t)} - \rho h A \omega^2 e^{i(kx - \omega t)} = 0 \quad (29)$$

This gives the frequency-wavenumber expression for flexural plate waves

$$\omega = k^2 \sqrt{\frac{D}{\rho h}}. \quad (30)$$

and, for $\omega = kc$, the dispersion relation

$$c = k \sqrt{\frac{D}{\rho h}}. \quad (31)$$

B. EXTENSIONAL WAVE

The governing equations for the extensional wave [Ref. 11], may be derived from the equations of motion

$$\frac{\partial \sigma_{ij}}{\partial x_j} + F_i = \rho \frac{\partial^2 u_i}{\partial t^2} \quad (32)$$

where a sum over repeated indices is intended. Assuming plane stress,

$\sigma_z = \tau_{xz} = \tau_{yz} = 0$, and neglecting out-of-plane body forces, $F_z = 0$, these reduce to

$$\frac{\partial \sigma_x}{\partial x} + \frac{\partial \tau_{xy}}{\partial y} + F_x = \rho \frac{\partial^2 u}{\partial t^2} \quad (33)$$

and

$$\frac{\partial \tau_{yx}}{\partial x} + \frac{\partial \sigma_y}{\partial y} + F_y = \rho \frac{\partial^2 v}{\partial t^2}. \quad (34)$$

Hooke's law is given as,

$$\sigma_{ij} = \lambda \varepsilon_{kk} \delta_{ij} + 2\mu \varepsilon_{ij}. \quad (35)$$

with

$$\sigma_{13} = 0 = 2\mu \varepsilon_{13}, \quad (36)$$

$$\sigma_{23} = 0 = 2\mu \varepsilon_{23}, \quad (37)$$

$$\sigma_{33} = 0 = \lambda(\varepsilon_{11} + \varepsilon_{22} + \varepsilon_{33}) + 2\mu \varepsilon_{33}. \quad (38)$$

By solving equation 38 for ϵ_{33} , the relationship to ϵ_{11} and ϵ_{22} is shown as

$$\epsilon_{33} = -\frac{\lambda}{\lambda + 2\mu}(\epsilon_{11} + \epsilon_{22}). \quad (39)$$

and with

$$\epsilon_{ij} = \frac{1}{2}\left(\frac{\partial u_i}{\partial x_j} + \frac{\partial u_j}{\partial x_i}\right) \quad (40)$$

equation (35) can be rewritten as

$$\sigma_{ij} = \frac{2\mu\lambda}{\lambda + 2\mu} \frac{\partial u_k}{\partial x_k} \delta_{ij} + \mu\left(\frac{\partial u_i}{\partial x_j} + \frac{\partial u_j}{\partial x_i}\right), \quad (41)$$

For conditions of plane stress this becomes

$$\sigma_x = \frac{2\mu\lambda}{\lambda + 2\mu}\left(\frac{\partial u}{\partial x} + \frac{\partial v}{\partial y}\right) + \mu\left(2\frac{\partial u}{\partial x}\right), \quad (42)$$

$$\tau_{xy} = \tau_{yx} = \mu\left(\frac{\partial u}{\partial y} + \frac{\partial v}{\partial x}\right). \quad (43)$$

and

$$\sigma_y = \frac{2\mu\lambda}{\lambda + 2\mu}\left(\frac{\partial u}{\partial x} + \frac{\partial v}{\partial y}\right) + \mu\left(2\frac{\partial v}{\partial y}\right). \quad (44)$$

Here Lamé's constants are given in terms of elastic modulus and Poisson's ratio as

$$\lambda = \frac{Ev}{(1+\nu)(1-2\nu)} \quad (45)$$

and

$$\mu = \frac{Ev}{2(1+\nu)}. \quad (46)$$

Lamé's constants are inserted into equations (42) , (43) and (44) . Upon differentiating these equations, the results are substituted into equations (33) and (34). With the body forces equal to zero, the governing equations for the extensional mode are as follows

$$\frac{\partial^2 u}{\partial x^2} + \frac{(1+\nu)}{2} \frac{\partial^2 u}{\partial y^2} + \frac{(1+\nu)}{2} \frac{\partial^2 v}{\partial x \partial y} = \frac{(1-\nu^2)\rho}{E} \frac{\partial^2 u}{\partial t^2} \quad (47)$$

and

$$\frac{\partial^2 v}{\partial y^2} + \frac{(1-\nu)}{2} \frac{\partial^2 v}{\partial x^2} + \frac{(1+\nu)}{2} \frac{\partial^2 u}{\partial x \partial y} = \frac{(1-\nu^2)\rho}{E} \frac{\partial^2 v}{\partial t^2}. \quad (48)$$

A solution of the form

$$u = Ae^{i(kx - \omega t)} \quad (49)$$

and $\nu=0$ is assumed. When this is substituted into the governing equations, the frequency-wavenumber expression for the extensional plate waves is given as

$$\omega = k \sqrt{\frac{E}{\rho(1-\nu^2)}}. \quad (50)$$

By substituting for $\omega=kc$,

$$c = \sqrt{\frac{E}{\rho(1-\nu^2)}} \quad (51)$$

it can be seen that the mode is dispersionless (velocity is independent of wave number k). Therefore, the dispersionless, extensional wave more accurately preserves the waveform generated by an event than the flexural wave. The concept of linear location to find the source of an AE event requires an accurate measurement of arrival times of the stress pulse at known locations. Consequently, depending on the source, the non-dispersive nature of the extensional wave when present provides a better waveform on which to base information on the time of arrival of propagating waves.

C. LINEAR LOCATION

The location of an AE source can be determined by measuring the time it takes for the wave to propagate between two sensors. For linear location, the concept is simple and is illustrated in Figure II.3. From this figure, it can shown that

$$t_1 = \frac{(L/2 - x)}{c} \quad (52)$$

and

$$t_2 = \frac{(L/2 + x)}{c} \quad (53)$$

The distance x from the source to midpoint between sensors is then given by

$$x = \frac{c(t_2 - t_1)}{2} \quad (54)$$

Calibration and verification of this concept were accomplished in this experiment by using an AE source of known location (lead breaks). Lead breaks were done inline opposite the sensors in order for the wave to travel the total distance, L , between the sensors in order to calculate Δt_{\max} . This provided the data needed to calculate wave speed (c). Given the distance between the two sensors (L) and the maximum difference in arrival time, the wave speed was determined by

$$c = \frac{L}{\Delta t_{\max}} \quad (55)$$

with Δt being the difference in the time of arrival at sensor 1 and the time of arrival at sensor 2. The times of arrival were measured using an oscilloscope. The leading edge of the extensional mode was taken to be the time of arrival. This resulted in a measured wave speed of $0.21 \text{ in}/\mu\text{s}$. Using a Poisson's ratio of 0.3, a Young's modulus of 73 GPa and a density of 2770 kg/m^3 for 7075 Al, equation (51) yields a calculated wave speed of 5380 m/sec or $0.21 \text{ in}/\mu\text{s}$. Thus the experimental results agreed with the theoretical computations.

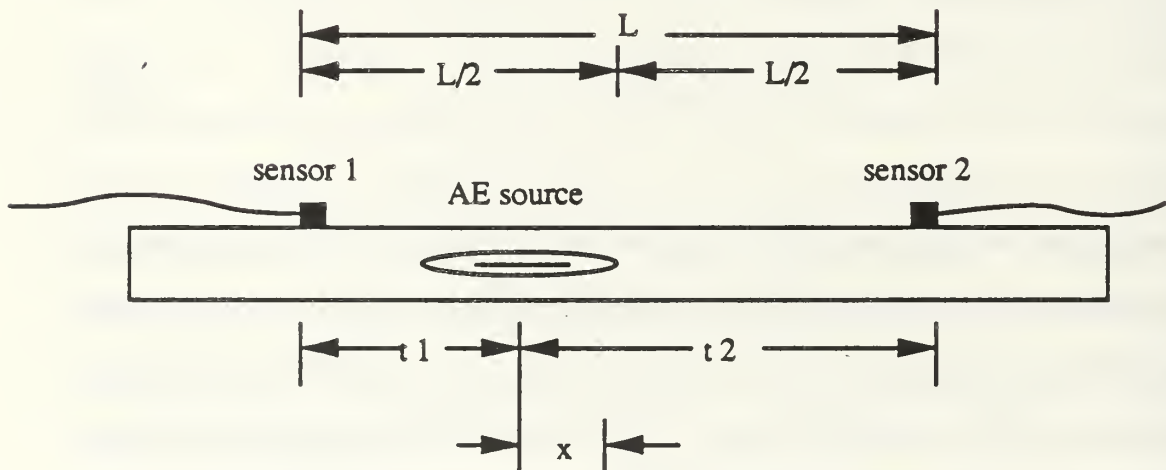


Figure II.3: Linear Location diagram

III. INSTRUMENTATION

A. EXPERIMENTAL SET-UP

Specimen testing was done in the Non-Destructive Evaluation (NDE) Lab of the Aeronautical Engineering Department at the U.S. Naval Postgraduate School. Specimens from a previous experiment which modeled the wing's main beam web section were modified for more complex acoustic emission testing than previously done. The specimens were tested under spectrum fatigue loading using a Materials Testing System (MTS) Model 810 testing machine. Each test was monitored using acoustic emission and video microscopy equipment. The system setup is shown in Figure III.1 and explained in the following sections.

B. SPECIMEN MODIFICATION AND SPECTRUM LOADING

The specimen used by Smith [Ref. 1] was a 4" wide by 14" long, 0.125" thick aluminum plate. The critical crack area in the main beam web is shown schematically in Figure III.2. The specimen modeled the lower portion of both the main beam web and fuel cell cutout, and the critical attachment hole in order to reproduce the stress conditions in the vicinity of wing station 49.

The modified specimen used in this experiment is shown in Figure III.3. Modeling the wing skin's junction to the web section, two cap angles were attached. The cap angles provided an interactive source of noise that may be encountered during certain aspects of flights (carrier arrestments, field landings, etc.) when severe loading of the web section takes place or during normal aspects of flight (i.e., engine/propeller vibrations, raising and lowering of landing gear or flaps, etc.). Figure III.4 shows the actual area of interest on the full-scale, fatigue test article.

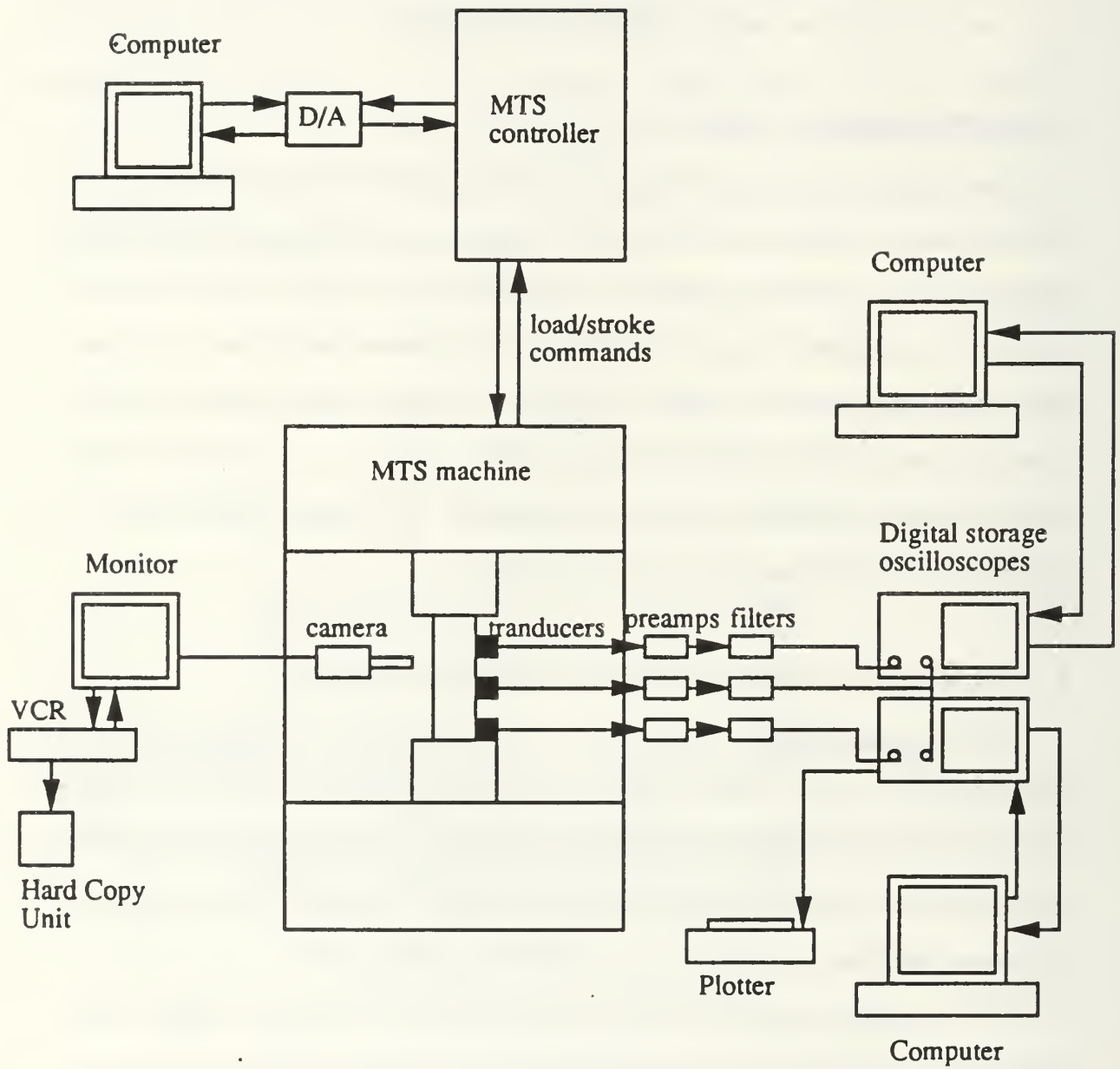


Figure III.1: Experimental Apparatus

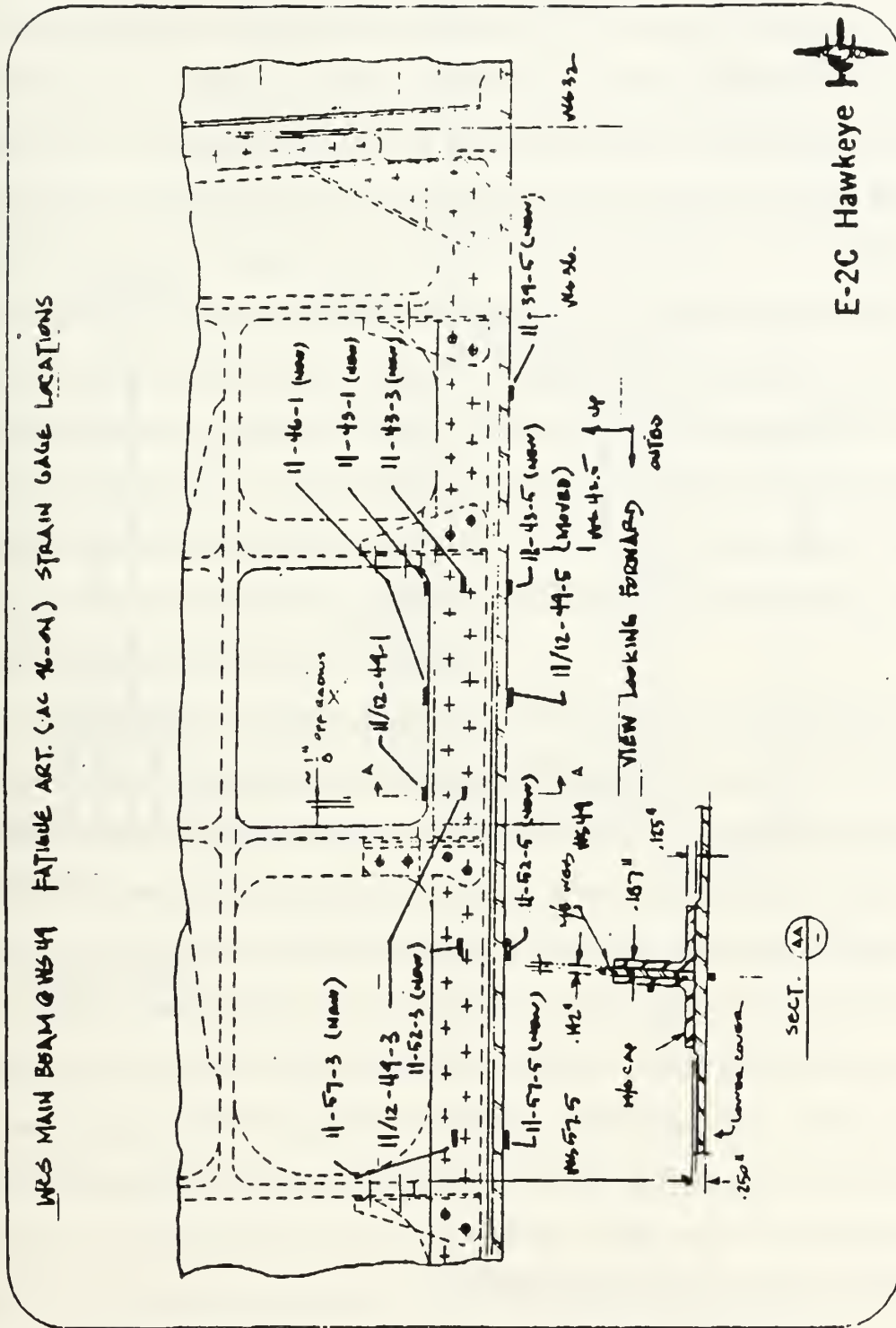
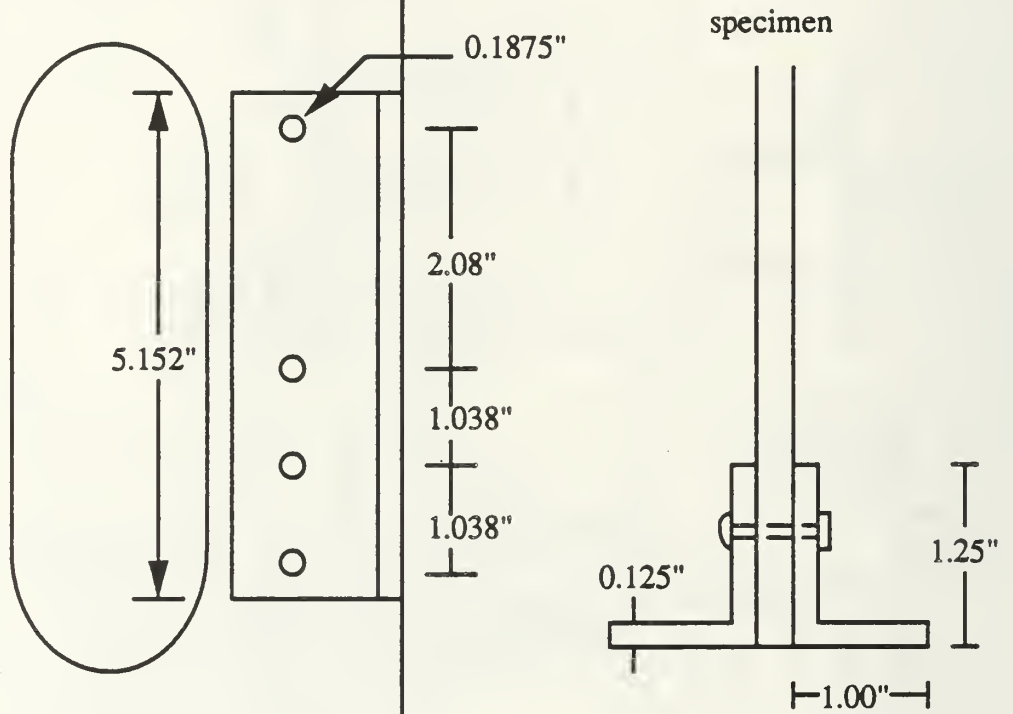


Figure III.2: WCS Main Wing Beam critical area



Modified Specimen

Figure III.3: Specimen with cap angles.

The specimens were constructed from 7075-T6 sheet aluminum (bare) of 0.125" thickness. This is the same material as the main beam web, only slightly thinner. The cap angles were cut from extruded structural shape (6061) aluminum of the same 0.125" thickness and were dimensioned similarly to the full-scale test article, however, the length was sized to enable the attachment of a sensor to the plate, between the cap angle and the machine grips. To attach the cap angles to the plate, three additional holes were drilled in line below the original hole and spaced from the lower cutout radius so as not to translate the stress concentration from the original attachment hole. In later testing this was found to be not true, however, an accurate reproduction of the stress state in the full-scale test article was not necessary for the successful operation of this experiment. For fasteners, 3/16 in. brass screws and aluminum nuts were used.

The same fatigue spectrum was used as that of Smith's experiments [Ref. 1]. This fatigue spectrum was based on Grumman's analysis of statistical data on types of missions flown and accelerometer readings from the E-2C aircraft. This provided a block of 500 experimental flight hours (EFH), which contained 12,493 load cycles. Of these, 6,818 cycles were dynamic landing loads, which cause approximately 90% of the fatigue damage. Each cycle consisted of a pair of loads, corresponding to the maximum and minimum load at that flight condition. These loads were expressed as a percentage of the average flight loading, or reference load. The stress level corresponding to this reference loading for the area of interest was 37,500 psi. Using minimum net cross-sectional area, the reference loading for the specimen was 13,209 lb. Each load percentage was multiplied by this reference load to generate a fatigue loading file that contained 13,636 loads (6,818 load pairs).

C. MECHANICAL TESTING EQUIPMENT

An MTS Model 810 closed-loop, servo-hydraulic testing machine was used in the testing. Modifications to the load frame for previously conducted experiments included remote mounting of the servo valve manifold, to isolate the frame from hydraulic switching and dither noise, and installation of a higher capacity servo valve to allow higher fatigue testing frequencies. Unmodified fatigue spectrum and computer programmed loading spectrums were used for the current work.

An 8086 based, personal computer programmed to supply the loading spectrum to the MTS controller was equipped with a digital-to-analog (D/A) board (Metrabyte DAS-16G) which supplied a digital word representing the desired load to the D/A board. The D/A board converted this digital word to an analog voltage in the range of 0 to 10V. This voltage was proportional to the desired load and was fed into the MTS controller. The controller compared this command with the load cell output and developed a voltage difference signal. This signal was then used to alter the specimen load to match the command load.

The specimen was held in place by a pair of grips constructed specifically for these specimens. These grasped the specimen using sliding jaws that were clamped in place and held the specimen by friction. To lessen the amount of slipping recorded by the previous testing, worn and damaged bolts were replaced by newer bolts. This did not eliminate all the noise at the grips and later it was determined that extraneous crack-like noise was originating from several cracks developing at the welded joints on the grips.

D. ACOUSTIC EMISSION INSTRUMENTATION

To monitor the acoustic emission produced during the test, 5 MHz broadband piezoelectric transducers (0.25" diameter Harisonic G0504) were used to capture the acoustic emission waves and two digital storage oscilloscopes (DSO) and personal computers were used to capture the entire waveform.

1. Transducers

The piezoelectric transducers used were sensitive to the normal component of the surface displacement caused by a traveling stress wave. These transducers were chosen because of their reasonably flat response to frequencies in the region below 1 MHz. It was extremely important to accurately measure the frequencies in the stress wave in order to discriminate between the extensional and flexural modes.

The transducers were attached to the specimen at locations similar to Figure III. 4 using Dow Corning high vacuum grease as an acoustic couplant and secured in place using electrical tape. The locations of the transducers varied with each test due to the configuration in which the specimen was being tested. When the cap angles were attached, transducer 2 was at first placed on top of the cap. It was found during lead break calibrations that this position for sensor 2 changed the shape of the wave, thus changing the wave arrival times needed for location analysis. It was then repositioned to the edge of the fuel cell cutout and lead break calibrations for this position showed correct arrival times (Figure III.5). By placing two of the transducers on either end of the line of holes, they would be the first transducers triggered by a wave arriving through the grips (extraneous noise). By placing the third transducer between hole #1 and hole #2, discrimination amongst holes could be accomplished. Transducer 2 was used as the trigger channel due to its proximity to all the holes.

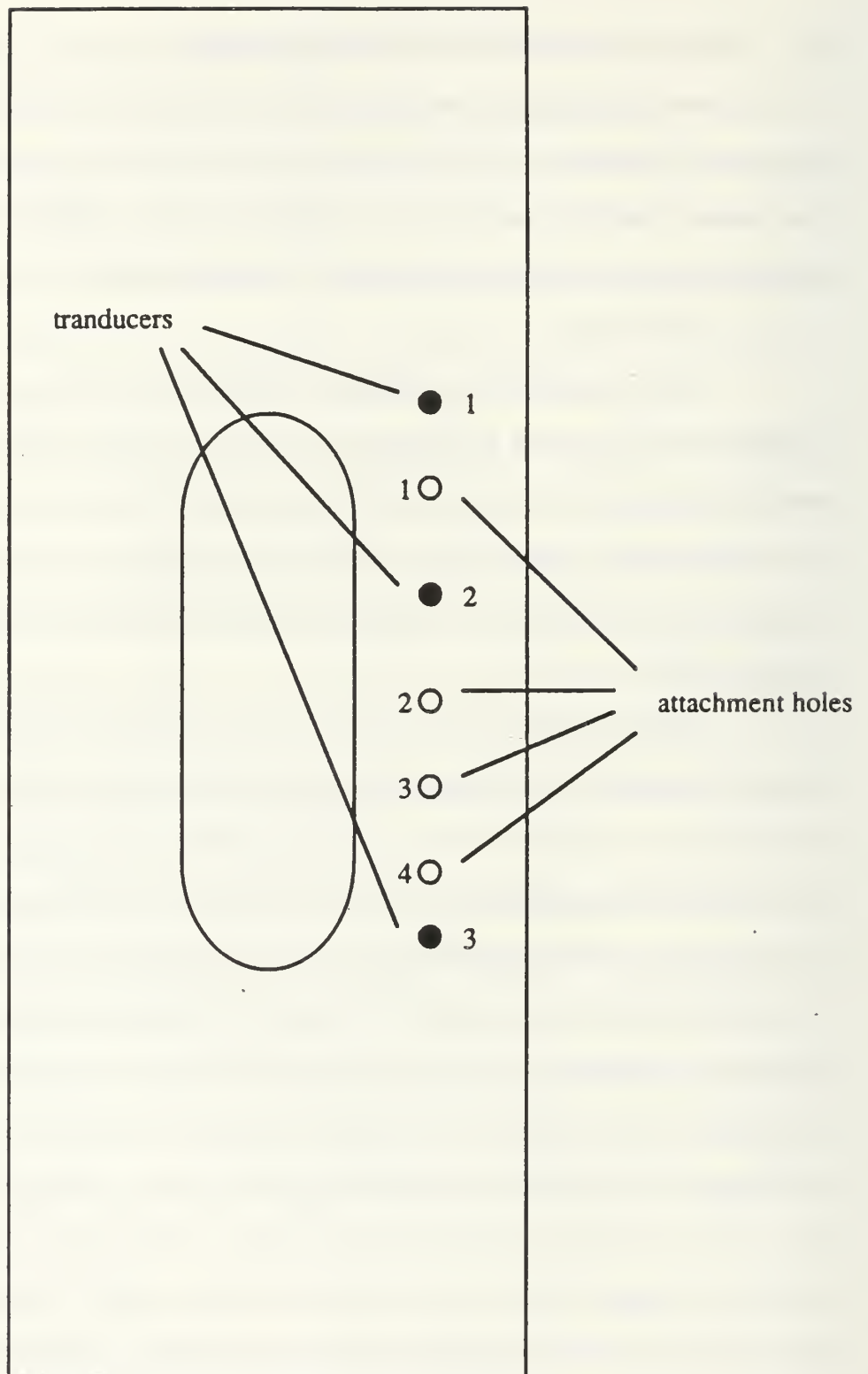


Figure III.4: Sensor Placement without cap angles.

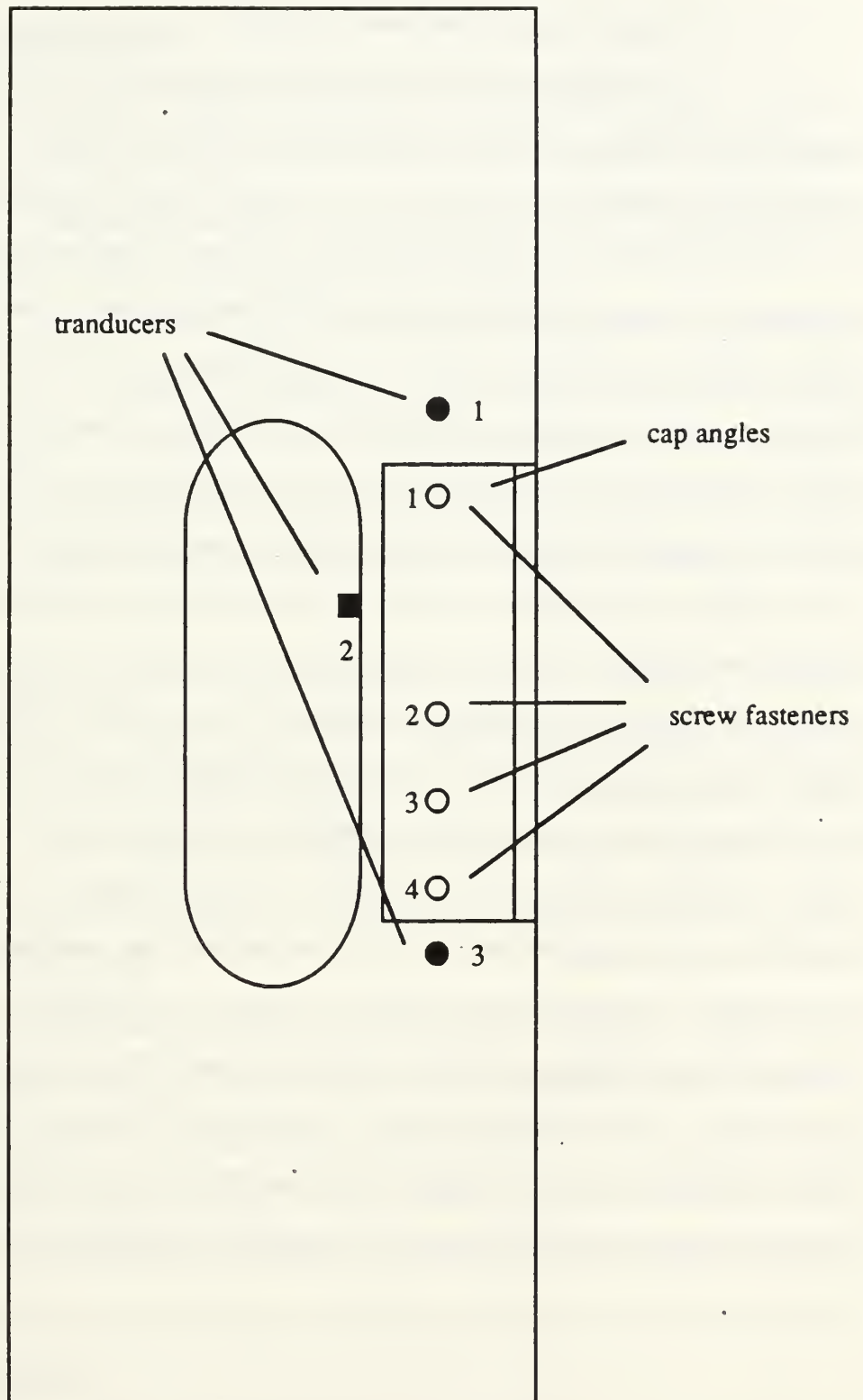


Figure III.5: Sensor placement with cap angles.

2. Digital Storage Oscilloscope (DSO)

Incoming signals from the transducers were first amplified by 60dB preamplifiers (Physical Acoustics Corporation 1220A) modified for broadband operation. The signals were then fed to two digital storage oscilloscopes (DSO's). The LeCroy 9400 digital storage oscilloscopes were used to capture, analyze, display and archive the waveforms. Built around a 68000 microprocessor, their two identical input channels are equipped with 100 megasample/second, 8-bit ADC's and 32 kiloword acquisition memories. The input from transducer 2 was split between both DSO's enabling sensor 2 to trigger both scopes simultaneously while transducers 1 and 3 were connected to their respective scope's remaining channel. Sensors 1 and 2 were displayed on channels 1 and 2 on the first scope, and sensors 3 and 2 displayed on channels 1 and 2 of the second scope. The captured data from each scope were passed to a dedicated computer. The two PC's (Compaq Deskpro 386/20's) used General Purpose Interface Bus (GPIB) boards for this data linking. The PC's used a mass storage program (MASP) provided by LeCroy to store and retrieve the data acquired by the DSO's. It also provided a remote control capability, storing triggered data from the scopes and then resetting the triggers. This enabled a hands-off data collection process that alleviated much of the workload. Post processing of the data allowed the recall of any waveform stored on the computer at which time Fast Fourier Transform (FFT) firmware built-in to the DSO's would allow frequency analysis of the waveforms. The waveforms could then be plotted using the RS-232-C plotter port connected to the HP-7470A Plotter.

E. VIDEO MICROSCOPY

The method used to verify crack growth in the specimen during testing was video microscopy. The setup contained the following components: video camera with high-power lens, high resolution monitor and double-reticle, time lapse video cassette recorder (SVHS VCR), and a video hard copy unit.

The camera used a 0.5" charged circuit device black-and-white video camera (Micro-Mac V-A). The camera was capable of 450 line horizontal resolution using a 610x488 pixel matrix. Attached to the camera was a 64x-400x zoom lens. The camera and lens were mounted on an X-Y-Z (left/right, up/down and focus in/out) camera mount, capable of remote control and fine adjustment scanning in 0.002" increments.

Video output was routed to a time lapse VCR for recording. The VCR (Panasonic Model AG-6720A-P) used a Super VHS recording format for 400 line resolution. Two features used for this test were the frame-by-frame viewing, necessary for a clear picture when paused for hard copy collection and a superimposed, elapsed time indicator to correlate AE events recorded by the DSO's and observed crack growth.

The monitor used was a Javelin Model BWM12, 12" black-and-white with an 800 line horizontal resolution. A video hard copy unit (Mitsubishi P-60U) was used for image processing. The unit used thermal heads to provide a 16 tone, gray scaled image with 400 line resolution using a 640x476 pixel matrix. The electronic double-reticle generator (Techni-Quip Model T-Q/DA) enabled the superimposing of crosshairs and frames on the image for measuring and monitoring crack growth at known magnifications.

The assembled video microscopy was found invaluable in the detection and monitoring of crack initiation and growth. For this test, acoustic emission

monitoring was not done until a crack was detected. Close monitoring of both inboard and outboard of all four attachment holes was necessary.

F. FILTERING

In tests involving the specimens without cap angles, most of the crack signals were discernible from the noise signals generated by the grips. Some noise signals did possess some of the higher frequencies characteristic of extensional waves, and in these instances digital filtering was explored. This consisted of a BASIC code that first transformed the output signal of the event using a fast Fourier transforms, then used a step function to filter frequencies requested by the user. Finally an inverse FFT was performed. This was effective on the flexural waves but distorted the initial response of the extensional waves, degrading the capability to measure the Δt 's needed for calculating a source location. This was a very tedious process in that each waveform needed to be loaded one at a time into the DSO's memory from the computer.

Specimens tested with cap angles contained not only noise from the grips but also large noise signals from the cap angles themselves. Due to the configuration and attachment method of the angles, excessive fretting and marring of the specimen occurred during the fatigue testing. These two unforeseen mechanisms produced large, low frequency flexural waves that saturated the DSO's displays and inhibited the detection of any crack signals, also making digital filtering useless. To prevent this, passive high-pass analog filters were constructed and positioned between the preamplifiers and the DSO's.

The crack signals were characterized by extensional waves in the 500 kHz and above range, therefore, a filter having a cutoff frequency that was below that of the lowest frequency in the signal needed to be constructed. Three filters were

constructed and tested before finalizing on one whose components produced the responses required.

Starting with the simplest of circuits, an RC filter was constructed consisting of one capacitor and one resistor [Appendix A, Figure A.1a]. The RC filter was designed around a 250kHz corner frequency using the equation

$$f_{3dB} = \frac{1}{2\pi RC} \quad (56)$$

As shown in Figure A.2, the input signal (upper trace) is compared with the output signal along with their FFT's (lower trace). Using this simple RC filter resulted in a -6dB/octave rolloff with a 250kHz corner frequency because the RC filter is based on a zero impedance driving source and an infinite impedance load.[Ref. 12]

A cascading RC filter [Figure A.1b] was constructed which produced a steeper rolloff, but the "knee" of the response curve did not sharpen. In Figure A.3, the cascading filter developed a -12dB/octave rolloff.

A filter design that could be optimized for maximal flatness of passband and a lower cutoff frequency was desired. By including inductors in the design, it is possible to create filters with any desired flatness of passband combined with sharpness of transition and steepness of rolloff outside the band. A 3-pole Butterworth design was decided upon due to it possessing these qualities [Figure A.1c]. The Butterworth filter produces the flattest passband response, at the expense of steepness in the transition region from passband to stopband. First, a 10μH inductor was used [Figure A.4]. This created the desired cutoff frequency but did not have the ideal flat passband response inherent in Butterworth filters. Figure A.5 shows the Butterworth with a 33μH inductor replacing the 10μH component.

This configuration brought about the needed cutoff frequency between 200-300kHz and the characteristic flat response of the Butterworth. As can be seen, this was a tremendous improvement over the RC filters.

Each filter was tested using a swept sinewave input, as shown in each of the figures, that was first fed through the preamplifiers set at +60dB gain, then through the filters and into the DSO's. The swept sinewave was generated using a LeCroy 9100 Arbitrary Function Generator that was triggered using a Wavetek 20MHz Pulse/Function Generator.

IV. RESULTS

A. LEAD BREAK CALIBRATIONS

The original concept of using lead breaks as an AE source was proposed by Hsu and Hardy [Ref. 13] and later refined by the National Institute of Standards. Lead breaks were used to create extensional and flexural waves in aluminum plates by Gorman [Ref. 9]. The use of lead breaks involves breaking a certain type of mechanical pencil lead (Pentel 2H, 0.3mm) to create an acoustic emission source very similar to the standard, glass capillary source used at the National Institute of Standards and Technology.

To analyze the lead breaks, a Fast Fourier Transform was performed on both the extensional and flexural waveforms, using the LeCroy 9400's built-in FFT firmware. The FFT was computed using 2500 data points with an effective sampling frequency of 2.5MHz. The results were displayed as a Power Spectrum (dB vs. Hz). The first calibration test was conducted on the modified specimen without cap angles attached. Figure B.1, Appendix B, shows a lead break conducted in hole 1 on the modified specimen without cap angles using preamplifiers set at 60dB gain and unfiltered with sensors configured as in Figure III.4. Breaking the lead in the hole produces in-plane crack-like signals whereas lead breaks on the surface of the specimen produce flexural noise-like signals. Due to similar wave speeds ($0.21\mu\text{s}$) calculated from arrival times between sensors 1, 2 and 3, and similar frequency content, it was concluded that the wave properties remained the same in the modified specimen. The plots show the signals from channels 1, 2 and 3 on the

center lines (voltage vs. time) in each plot, and at the bottom of each plot the frequency distribution (dB vs. kHz) for that particular wave is given.

To verify calculated arrival times, four lead breaks were conducted at each hole, two inboard and two outboard. Inboard refers to the radius closest to the fuel cutout and outboard refers to the radius closest to the specimen's edge. Using the DSO's, arrival times were measured by placing a cursor at the first deflection on the leading edge of the extensional wave for each trace. The measured arrival times were then compared to calculated arrival times. An example of calculated arrival times for the sensor configuration in Figure III.4 is shown in Table IV.1. Column one refers to the DSO displays. Each DSO displayed the signals from two sensors. The first DSO displayed the signals from sensor 1 and 2 on channels 1 and 2, respectively. The second DSO displayed signals from sensor 3 and 2 on channels 1 and 2, respectively. By placing the cursor at similar positions on the display from channel 2 on both DSO's, the arrival time between channels 1 and 3 could be measured. The second column refers to the difference in the distance from the hole to either sensor. This distance divided by the wave speed resulted in the calculated arrival times (column three). The $\pm 1\mu\text{s}$ error was based on sensor diameter and measurement of sensor location. The measured arrival times were found to agree with the calculated arrival times of the extensional mode.

If the arrival times of any signal measured during a fatigue test did not match those shown in column three, the signal was assumed to be from extraneous noise.

Next, lead break calibrations were conducted with the cap angles fastened to the specimen. In order to compare results between specimens with cap angles and without cap angles, lead breaks were conducted in the same manner as previously

TABLE IV.1 LEAD BREAK, TEST III, LEAD\T001.TRA

LEAD BREAK DISPLAY CALCULATIONS		
HOLE 1		
Channels	ΔL (in.)	Δt ($\pm 1 \mu s$)
1 - 2	0.580	2.76
2 - 3	3.826	18.22
1 - 3	5.406	25.74
HOLE 2		
1 - 2	1.580	7.52
2 - 3	2.826	13.46
1 - 3	0.246	1.17
HOLE 3		
1 - 2	1.580	7.52
2 - 3	0.250	1.19
1 - 3	1.830	8.71
HOLE 4		
1 - 2	1.580	7.52
2 - 3	2.288	10.89
1 - 3	4.656	22.17

mentioned using the same sensor configuration. Removing a fastener from its hole allowed inboard and outboard lead break was to be done in the hole. Each fastener was removed in turn and lead breaks were performed. As discussed in Chapter III, section D.1, transducer 2 was first placed on the cap angle at the same spacing as previously used for the uncapped specimen. As the wave propagated through the cap angles, the shape of the wave changed. The presence of the cap angles influenced the wave propagation and the measured arrival times were not in agreement with the times calculated previously for the uncapped specimens. Figure B.2 shows the signals from a lead break in hole 1 with transducer 2 placed on the cap angle. A comparison of the arrival time of $5\mu\text{s}$ between channels 1 and 2 and the calculated arrival time from Table IV.1 shows the discrepancy. This effect was demonstrated numerous times even by lead breaks in the other holes.

Repositioning transducer 2 to the edge of the fuel cutout (Figure III.5) yielded arrival times consistent with the uncapped specimens. Figure B.3 shows the signal responses of the sensors and the measured times of arrival of $3\mu\text{s}$, $18\mu\text{s}$ and $23\mu\text{s}$. These arrival times matched those calculated for this sensor configuration and lead breaks in hole 1. Due to its position on the edge of the fuel cutout, sensor 2 now measured the in-plane displacement component of the extensional mode. The large response seen in channel 2, (Figure B.3), reflects the fact that for the extensional mode, the in-plane displacement is much greater than the out-of-plane displacement. Subsequently, this transducer configuration was used for all tests with cap angles attached.

Now that a sensor configuration was established for both testing with and without cap angles, calibration lead breaks were performed to determine the effects of the electronic filtering. Figure B.4 shows the filtered signals without the cap angles. Comparing these plots with Figure B.3, it can be seen that much of the lower

frequency content of the waveforms has been eliminated, as was desired. Figure B.5 shows the filtered signal with cap angles attached. These signals also show that much of the lower frequency content has been eliminated. The filters did not affect the arrival measured arrival times.

B. CRACK GROWTH AND SIGNAL LOCATION

Three modified specimens were individually fatigued until a crack was visually identified in one of the attachment holes. Each specimen was then monitored using the experimental setup discussed in Chapter III. From previous experiments, crack initiation was known to occur after approximately 390,000 cycles (14,000 experimental flight hours). Specimens were fatigued to this number of cycles and then closely observed for crack growth by video microscopy. Once a crack was identified, in any of the holes, acoustic emission testing commenced. Each specimen produced cracks in each attachment hole. Due to the multiple crack locations, crack growth observation was difficult.

Test Specimen III (TSIII) attachment hole cracks and approximate crack lengths are displayed in Figures C.1a and C.1b. As seen in Figure C.1b, the crack in attachment hole 4 (TSIII) was the most advanced, however, visual crack growth and captured acoustic emission correlation were established while monitoring the crack at attachment hole 3. Figures C.2-5 show two separate events (crack growths) at attachment hole 3. Computers, DSO's and VCR were synchronized so as to correlate AE events with video recording. Figure C.2 shows before and after pictures of crack growth at 70x magnification. Figure C.3 shows captured signals from sensor's 1, 2 and 3. Signals were captured with preamplifiers set at 60 dB gain with the scope vertical resolution set to 0.1 V/div. for an effective gain of 80 dB at 1V threshold. However, the 3-pole Butterworth filters attenuated the signal by 10dB

resulting in an effective gain of 70 dB. Calculated ΔL and Δt for a source originating at hole 3 were 2.5 in. and 11.9 μ s between sensors 1 and 2, respectively, and 0.25 in. and 1.19 μ s between sensors 2 and 3, respectively. Measured times between channels 1 and 2 were 11 μ s and between channels 2 and 3, 2 μ s, verifying the location of the AE source to be at attachment hole 3. Figure C.4 shows an event 4.25 seconds later at the same attachment hole. Signals captured from this event are displayed in Figure C.5 with identical arrival times of 11 μ s and 2 μ s measured from channel's 1-2 and 2-3 respectively. These correlation's established a basis upon which other testing could be verified. It also confirmed earlier perceptions:

- Captured AE events with cap angles attached (i.e., no means of visual confirmation) were indeed crack growth signals.
- High frequency extensional waves were characteristic of crack growth signals.
- Crack growth could be detected acoustically at 70 dB.
- Filtering did not interfere with wave propagation velocity measurements.

Next, captured noise signals were examined and the difference in frequency content compared with that of crack signals. Figure C.6 shows typical unfiltered noise signals from sensors 1, 2 and 3 of TSIII without cap angles. The measured arrival times of 16 μ s between channels 1 and 2 and 15 μ s between channels 2 and 3 do not equate to the calculated arrival times of crack signals at any attachment hole. All unfiltered signals were captured using 0.1 V/div. and preamplifiers set to 60 dB gain. Figure C.7 shows the FFT's of the captured noise signals. Here the low frequency content that is characteristic of flexural waves in noise-like events can be seen. Figure C.8 shows noise signals from TSIII with cap angles attached. The large amplitudes are mainly due to the fretting and marring that occurred with the cap angles attached. The screen saturation made it impossible for accurate FFT's to be

calculated. Figure C.9 shows the damage to the specimens caused by the cap angles. The picture at the top of Figure C.9 shows hole 1 prior to attachment of the cap angles and the bottom picture shows the same hole after testing with the cap angles attached. Notice the gouging near the radius of the attachment hole. This produced several noise signals with arrival times nearly equal to arrival times of crack signals at that hole. The 3-pole Butterworth filters eliminated these noise signals. Figure C.10 shows a crack signal from attachment hole 1 in TSIII unfiltered and without cap angles. Measured arrival times of $4\mu\text{s}$ for channels' 1-2 and $18\mu\text{s}$ for channels' 2-3 agree with calculated times for that attachment hole. The lower half of the plots are the FFT's calculated for the signal. Here lower frequency components can be seen in the signal since no filtering was performed. These plots were compared to the testing done by Smith [Ref. 1]. Similar frequency content was seen between these FFT's and the FFT's found on page 65, Figure V.5b of Ref. 1. Figure C.11 displays the unfiltered crack signal from attachment hole 3 with cap angles attached, while Figure C.12 displays the unfiltered crack signal from attachment hole 4 with cap angles. With sensor placement remaining constant for both events, notice the difference in arrival times. Channels 1 and 2 arrival times are the same for both events, $11\mu\text{s}$. This is due to the event occurring outside the area between sensors 1 and 2. Arrival times for channels 2 and 3 for hole 3 was $1\mu\text{s}$ while times for hole 4 were $8\mu\text{s}$. Both events occurred between sensors 2 and 3, however, the crack in attachment hole 3 was approximately equidistant from both sensors, therefore the wave propagated nearly the same distance, triggering both sensors almost simultaneously. Figure C.13 shows the FFT's of the signal from attachment hole 4 (see Figure C.12). These plots show the higher frequency content characteristic of the extensional waves found in crack signals.

Figure C.14 displays the filtered crack signals and FFT's from attachment hole 3. The small amplitude of the signals is due to the 10dB attenuation typical of the 3-pole Butterworth filters used. The arrival times correspond with those of the crack in attachment hole 3 as seen in Figures C.3, 5 and 11.

V. CONCLUSIONS

The ability of linear location and analog filtering techniques to distinguish between multiple cracks and extraneous noise signals was demonstrated in this work. The filtering techniques were used to eliminate much of the noise created by cap angles attached with fasteners to specimens designed to simulate the web section of the E-2C Hawkeye main wing beam. Previous work by Smith [Ref. 1] demonstrated that AE signals due to crack growth were in the form of extensional waves and established a detectable crack length of 0.005" in 7075-T6 aluminum. The present work has built on this by using acoustic emission testing techniques on a noisier specimen. This experiment has verified several concepts, specifically:

- It has experimentally shown that extensional waveforms were detectable in a noisier specimen than previously tested.
- It has demonstrated optimum sensor placement for linear location techniques for this model.
- It has demonstrated the use of simple filtering techniques for the elimination of extraneous noise signals.

The model constructed did not accurately represent the full-scale test article. The cap angles caused fretting and marring of the specimens' surface producing false signals and unacceptable noise that saturated the oscilloscopes. This prevented accurate detection of the crack signals. By using precision machined cap angles to prevent the fretting and shear-head rivets as opposed to the machine screws and nuts, a more accurate model could be tested with less configuration induced noise.

Additional testing in this area would incorporate the results from this work and apply this technique to the monitoring of cracks in a full-scale fatigue article. Continued research in this field will lead to the development of practical monitoring of critical areas encouraging higher standards of quality control and more efficient use of preventive maintenance.

APPENDIX A: FILTERS

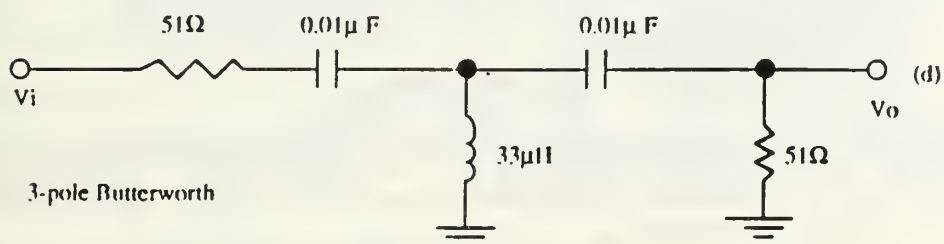
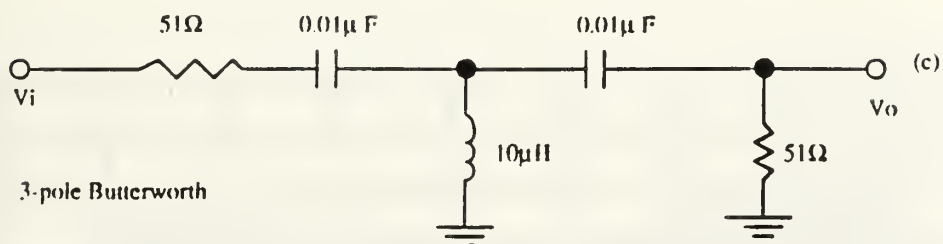
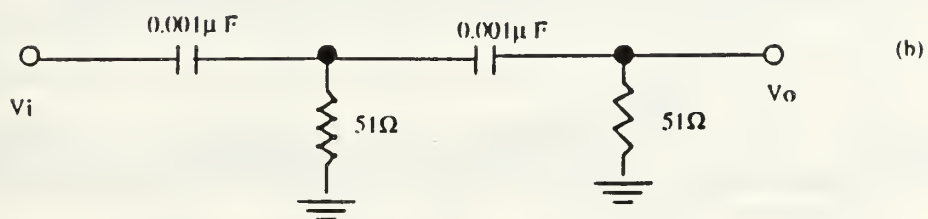
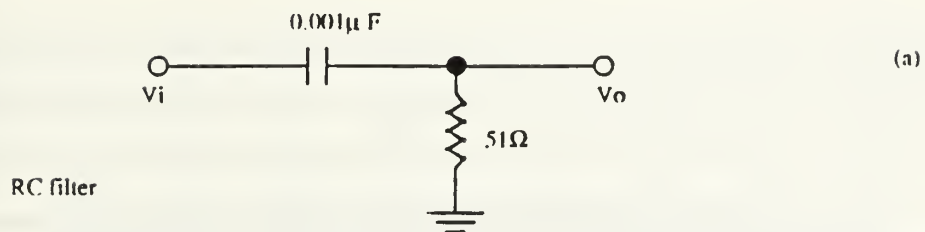


Figure A.1: Filter schematics

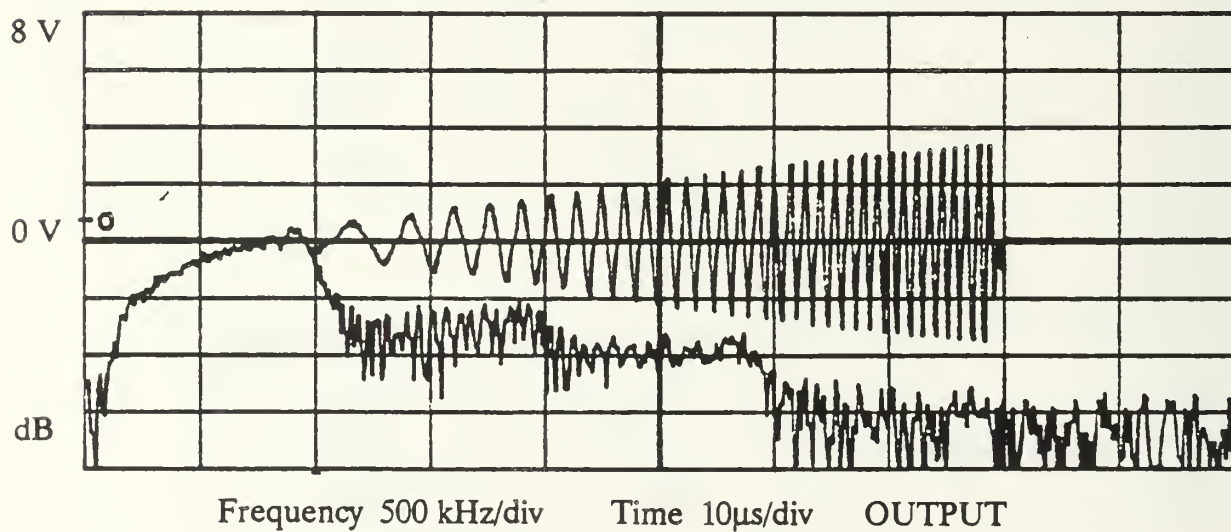
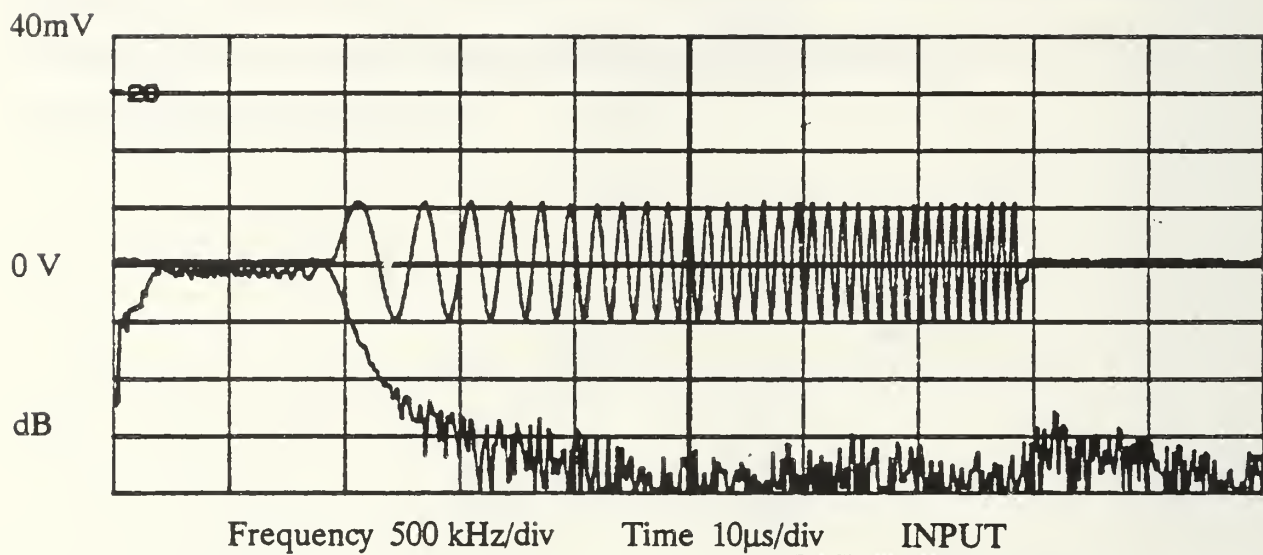


Figure A.2: RC filter

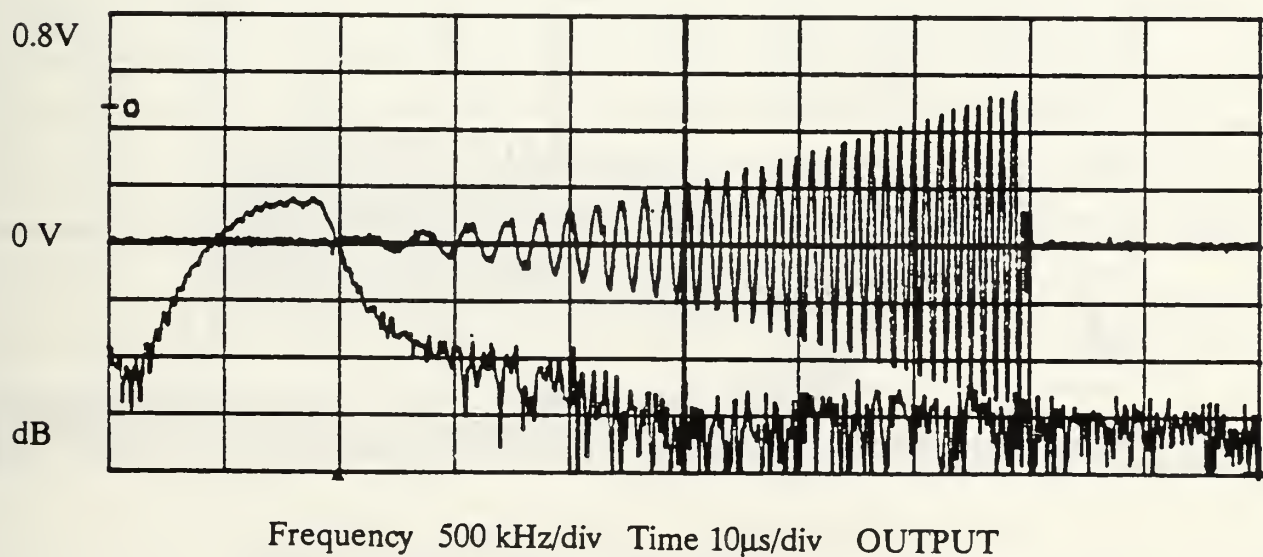
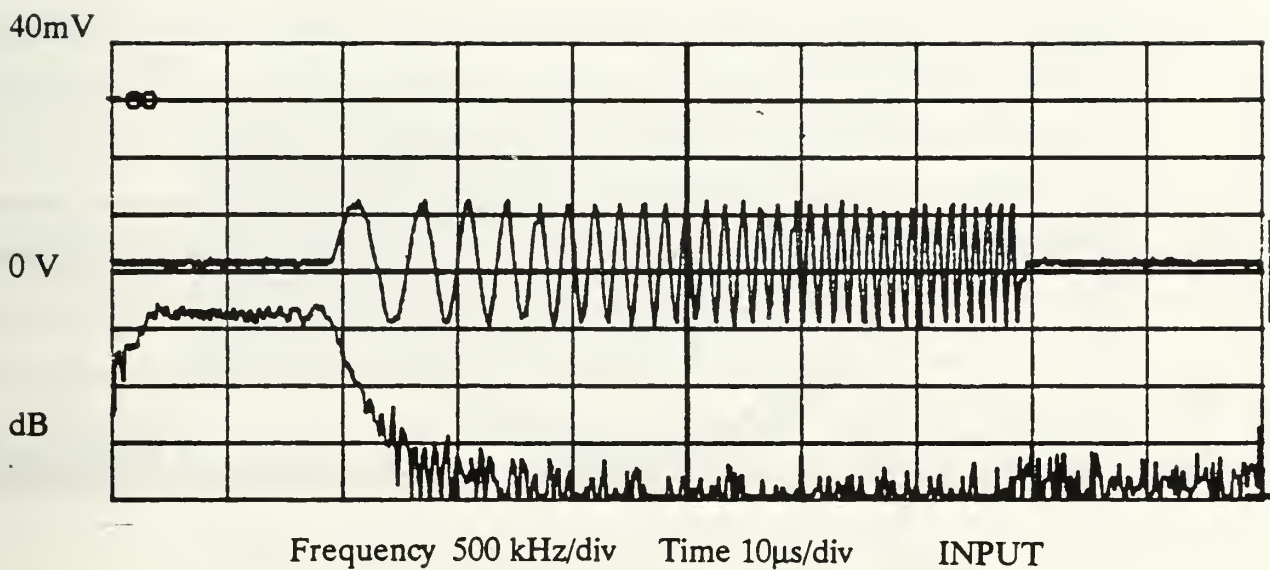


Figure A.3: Cascading RC filter

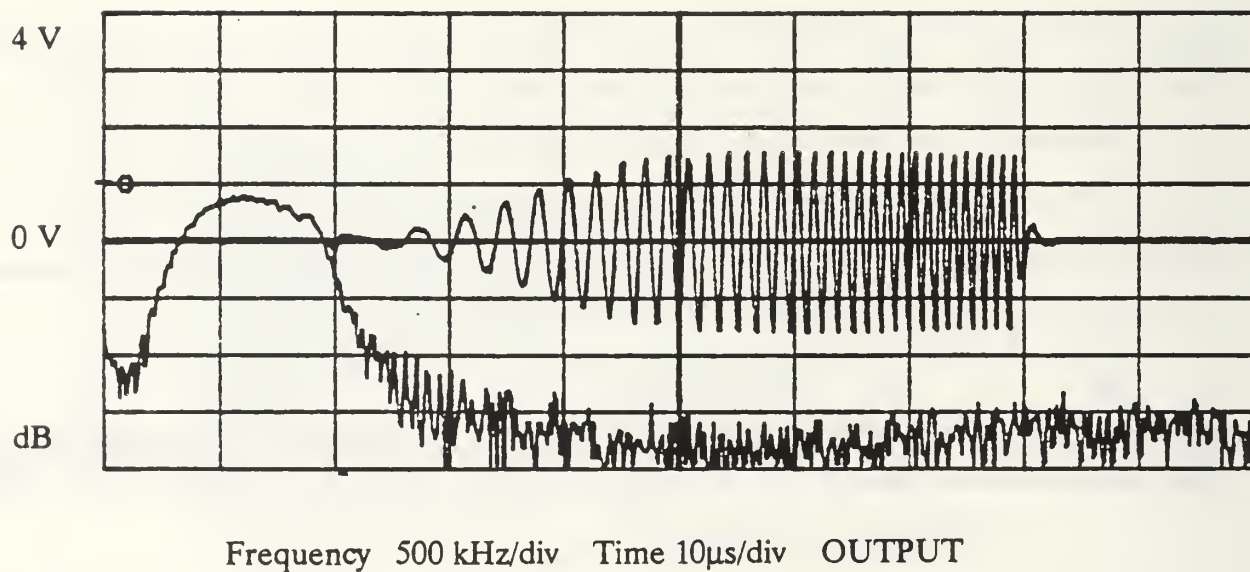
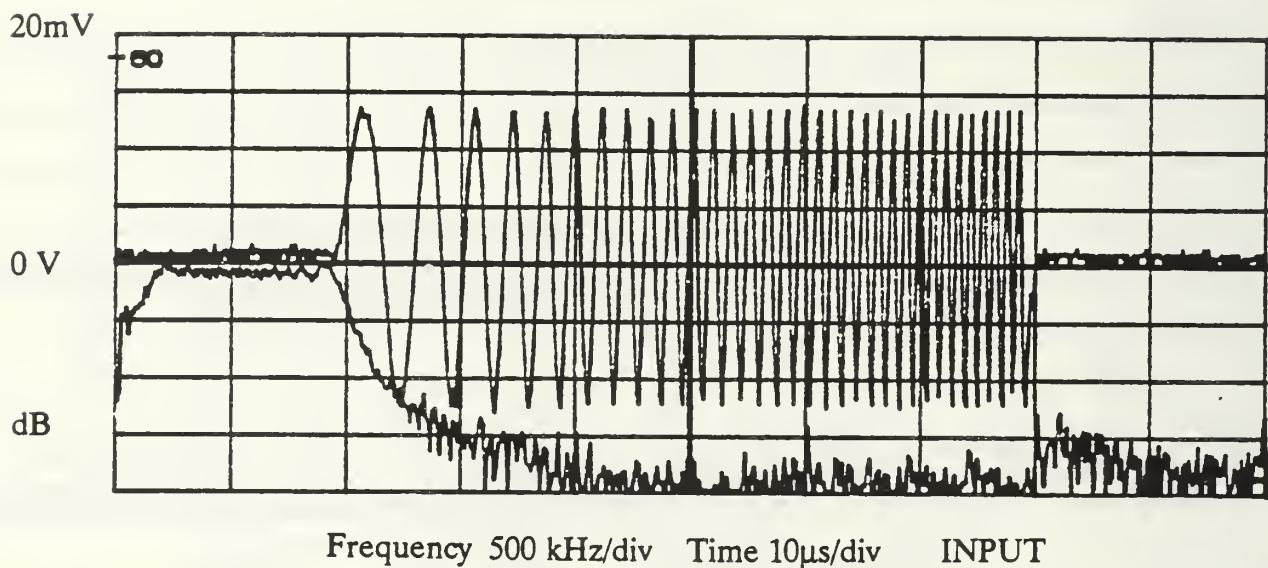
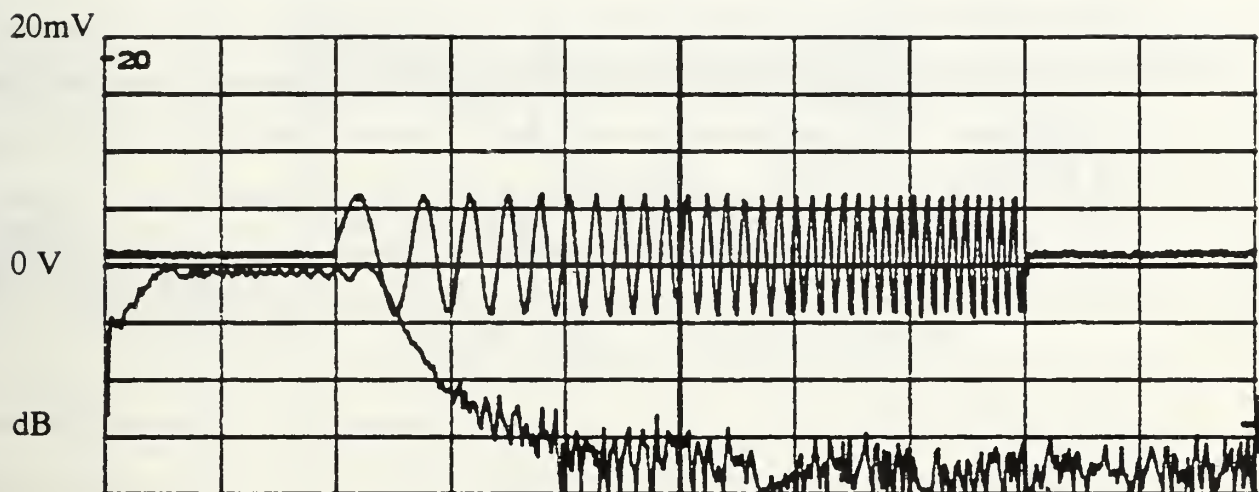
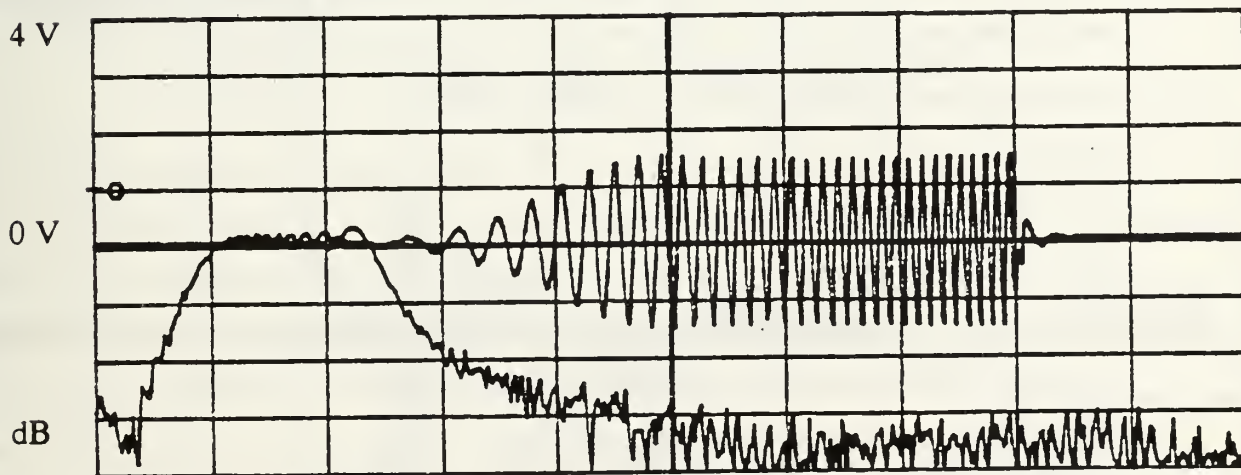


Figure A.4: 3-Pole Butterworth filter (10 μ H)



Frequency 200 kHz/div Time 10 μ s/div INPUT

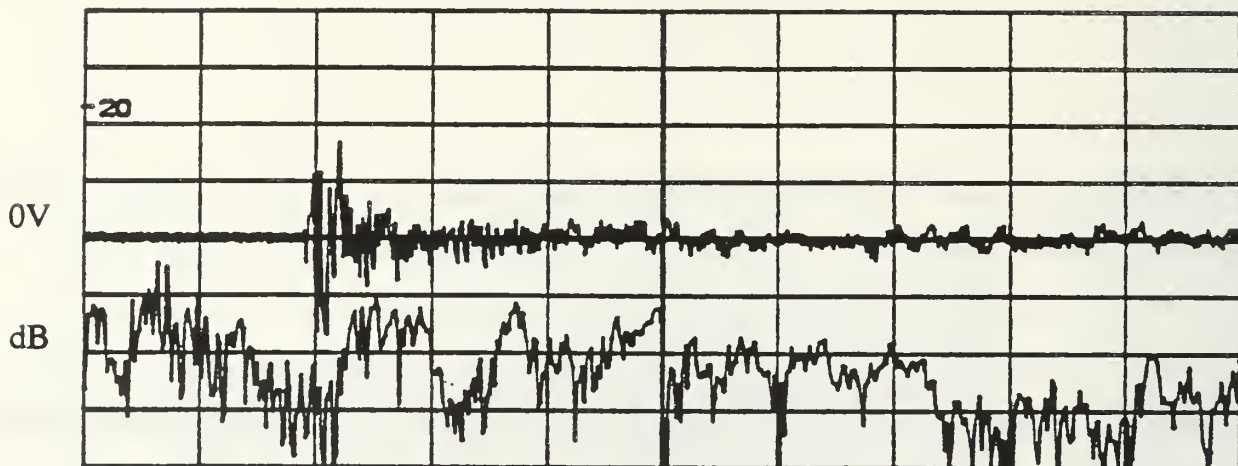


Frequency 200 kHz/div Time 10 μ s/div OUTPUT

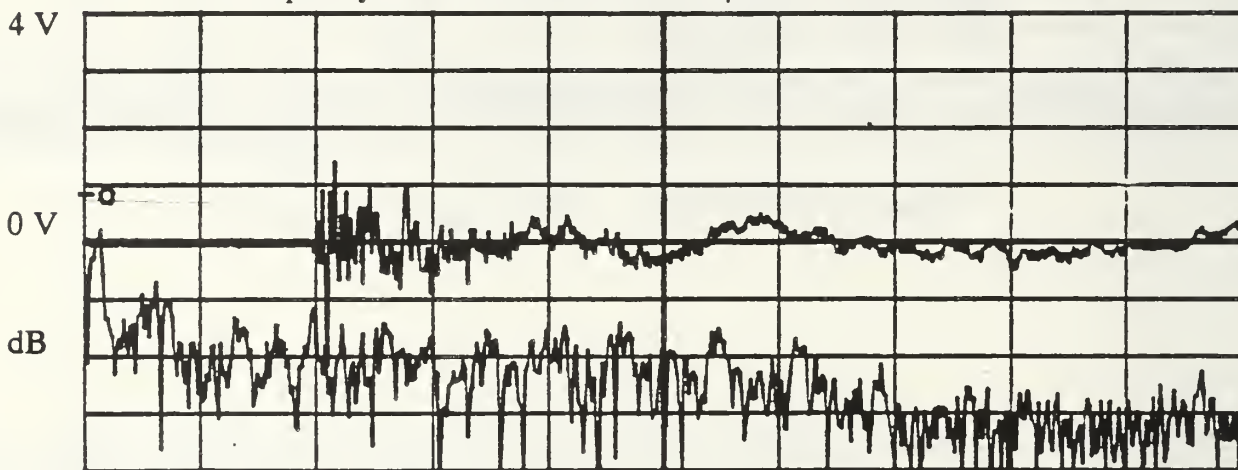
Figure A.5: 3-Pole Butterworth filter (33 μ H)

4 V

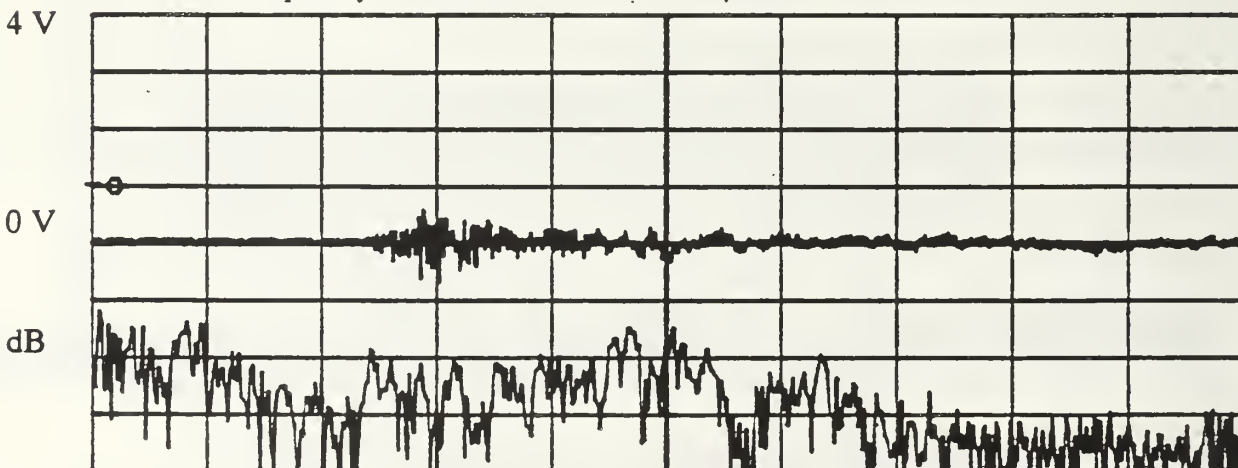
APPENDIX B: LEAD BREAKS



Frequency 100 kHz/div Time 50 μ s/div CHANNEL 1

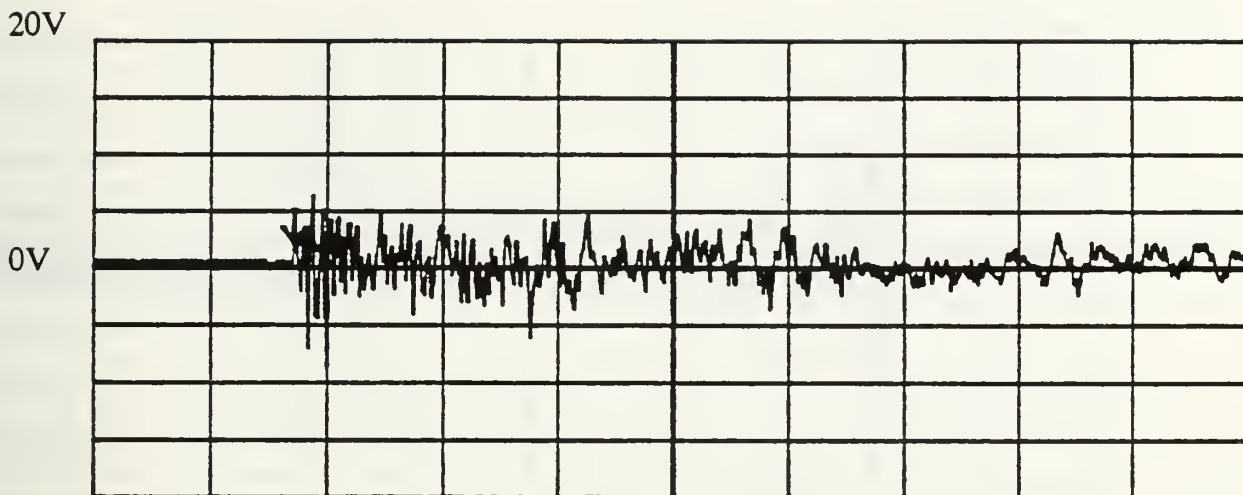


Frequency 100 kHz/div Time 50 μ s/div CHANNEL 2

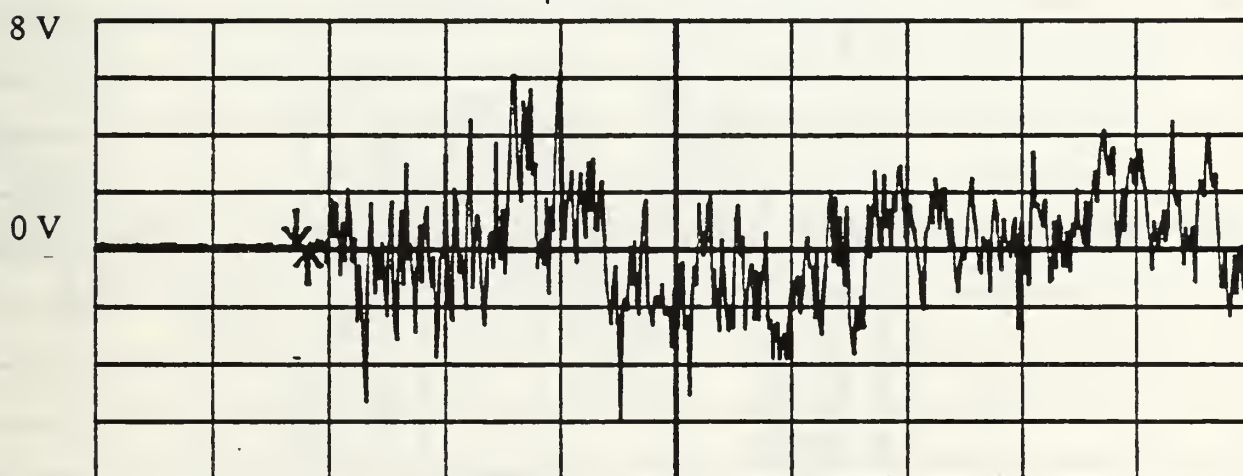


Frequency 100 kHz/div Time 50 μ s/div CHANNEL 3

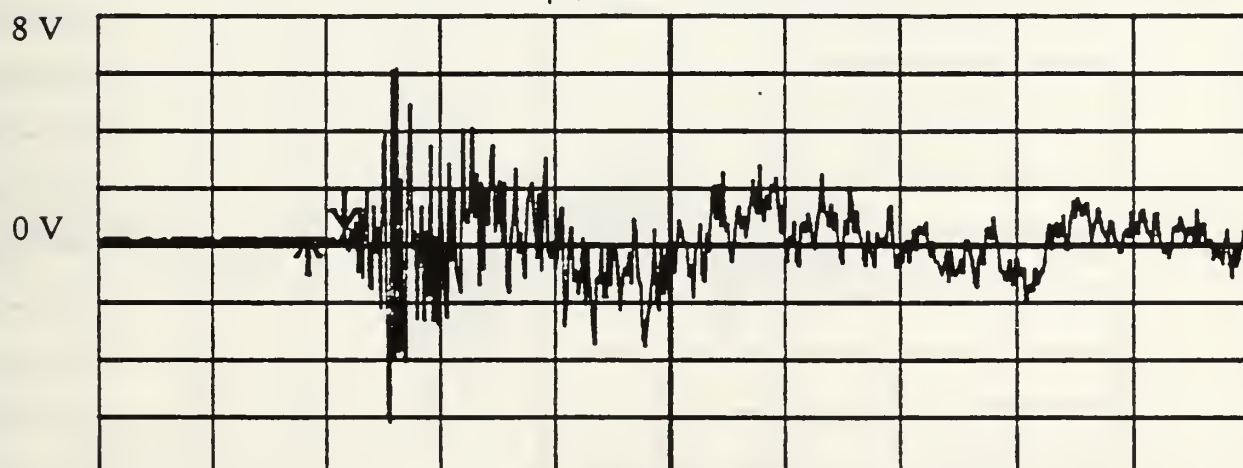
Figure B.1: Lead break, hole 1, unfiltered, without cap angles.



Time 50μs/div CHANNEL 1



Time 50μs/div CHANNEL 2

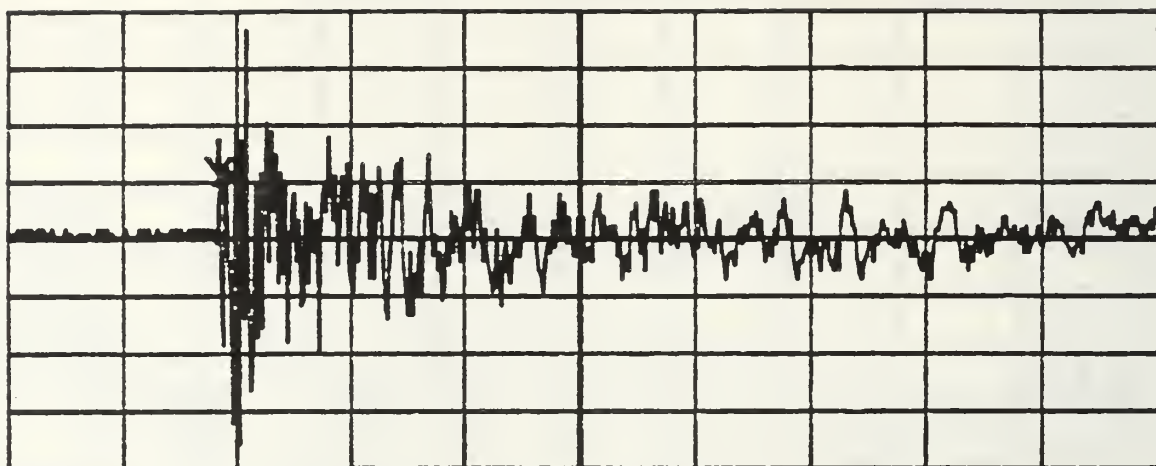


Time 50μs/div CHANNEL 3

Figure B.2: Lead break, hole 1, unfiltered, with cap angles, sensor on cap angle.

20V

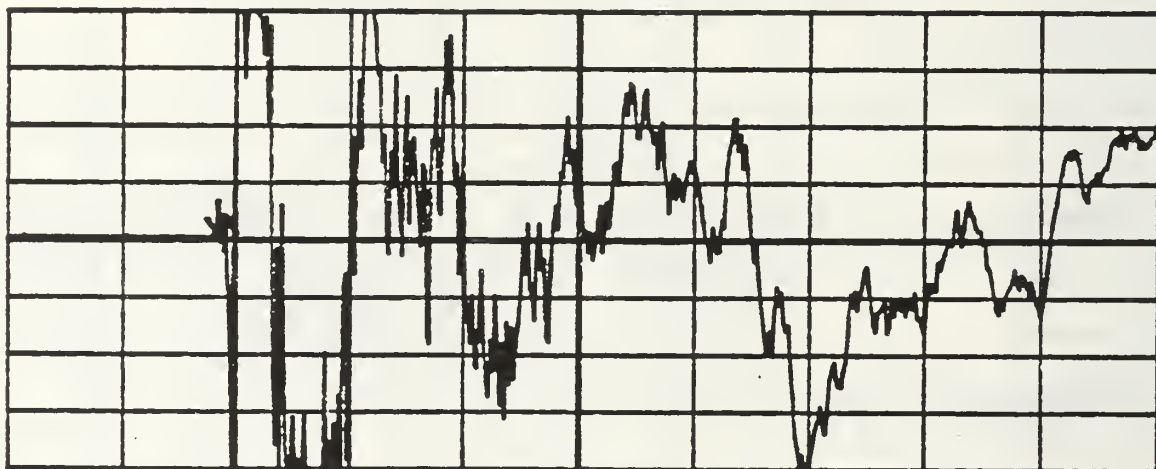
0V



Time 50 μ s/div CHANNEL 1

8 V

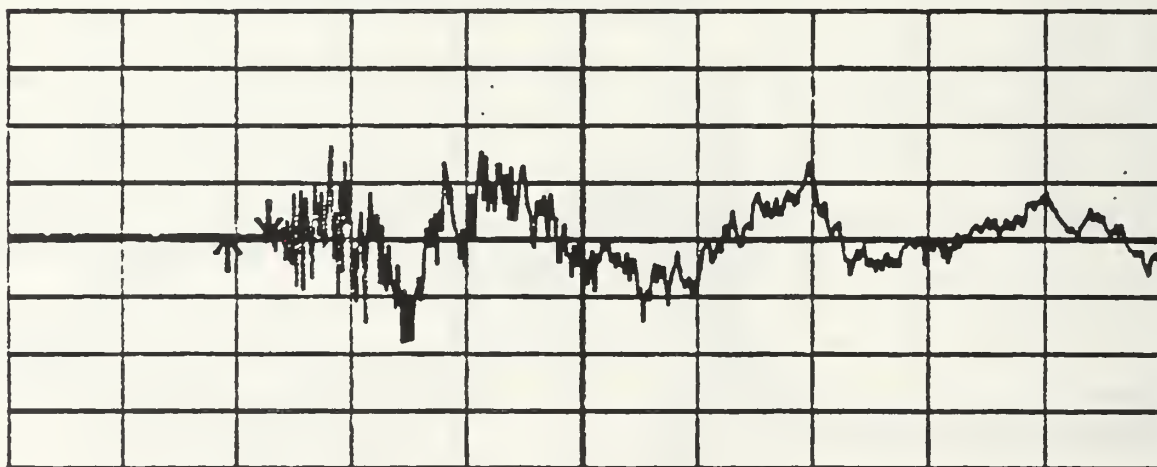
0 V



Time 50 μ s/div CHANNEL 2

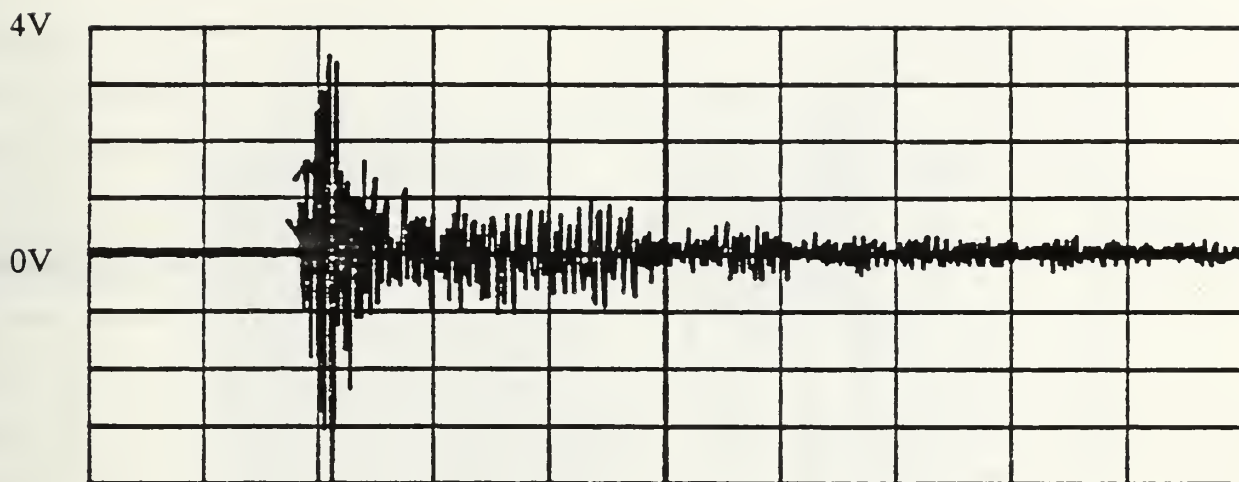
8 V

0 V

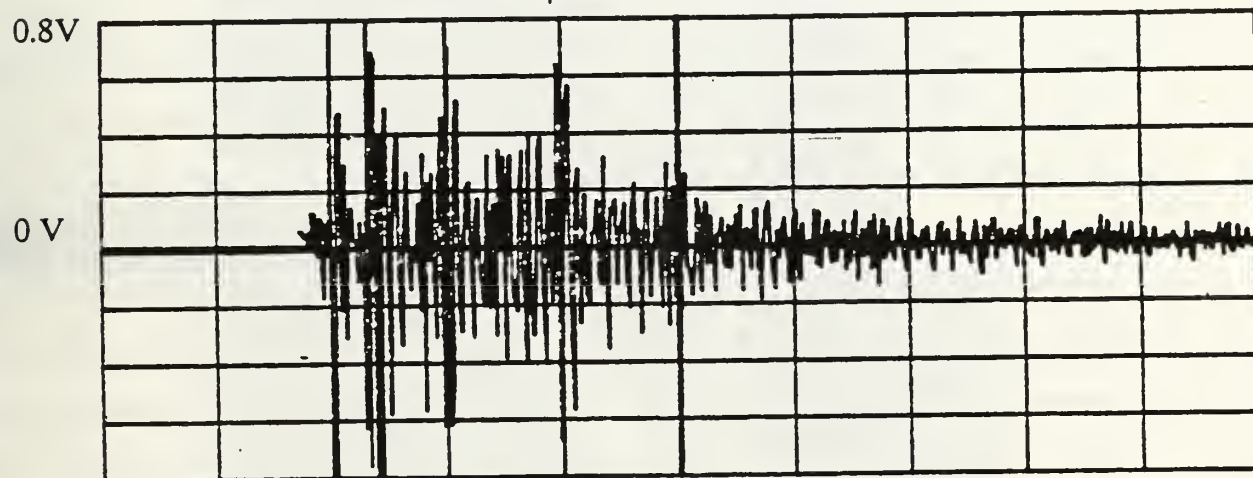


Time 50 μ s/div CHANNEL 3

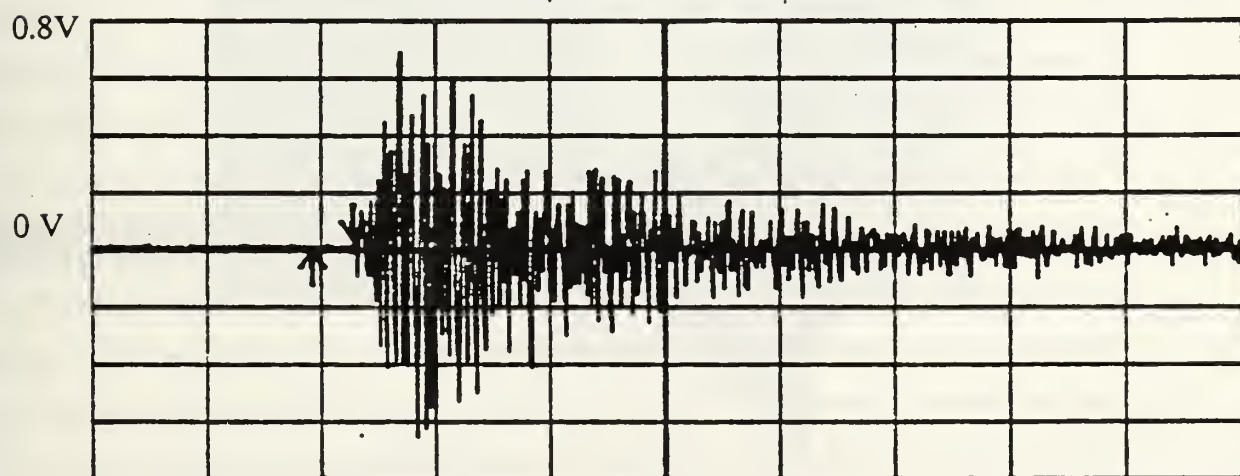
Figure B.3: Lead break, hole 1, unfiltered, with cap angles, sensor on cutout.



Time 50 μ s/div CHANNEL 1

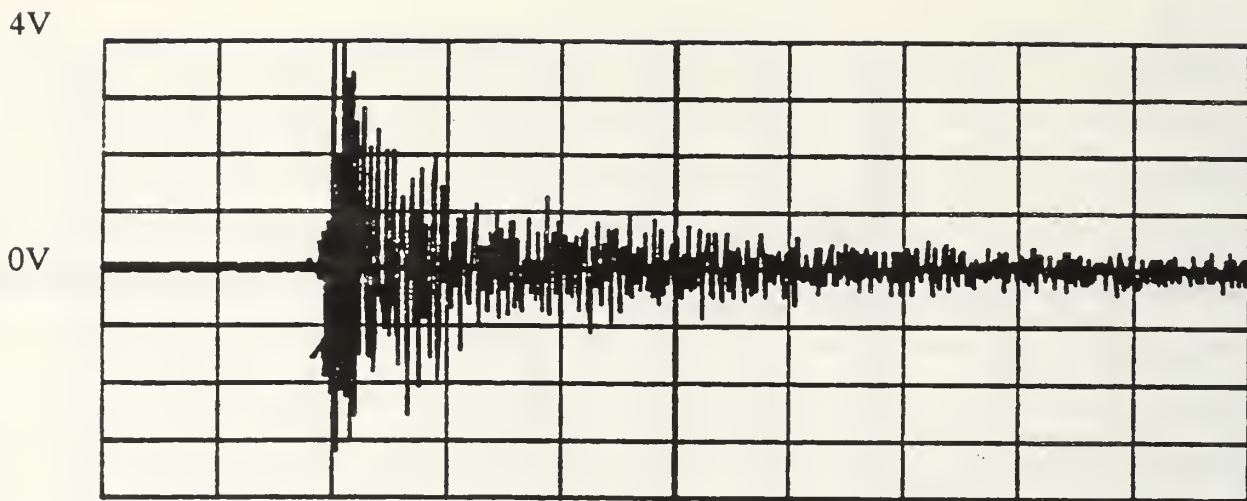


Time 50 μ s/div CHANNEL 2

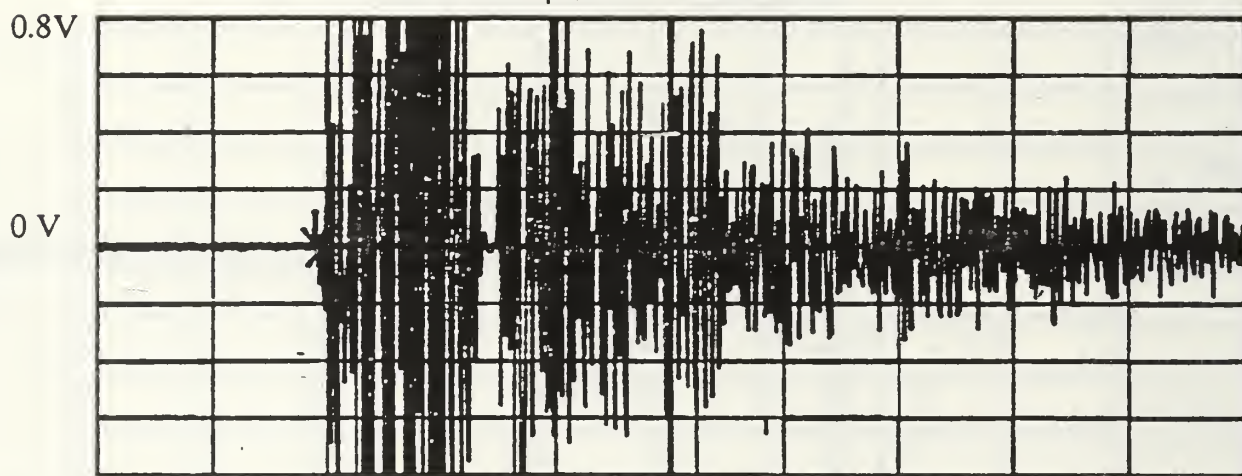


Time 50 μ s/div CHANNEL 3

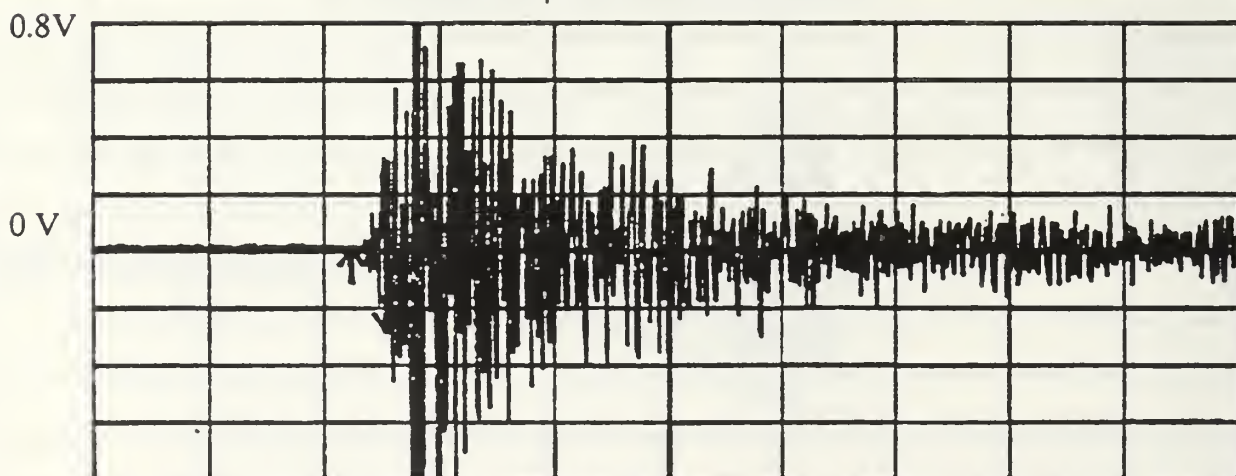
Figure B.4: Lead break, hole 1, filtered, without cap angles.



Time 50 μ s/div CHANNEL 1



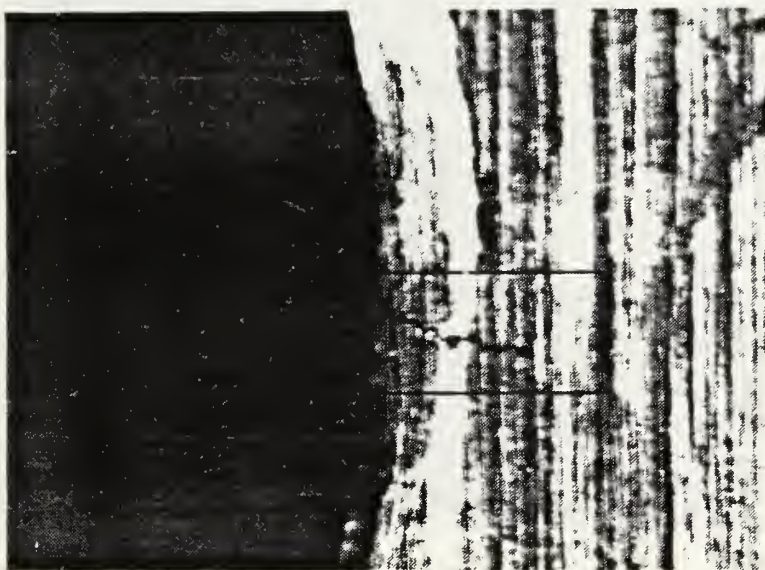
Time 50 μ s/div CHANNEL 2



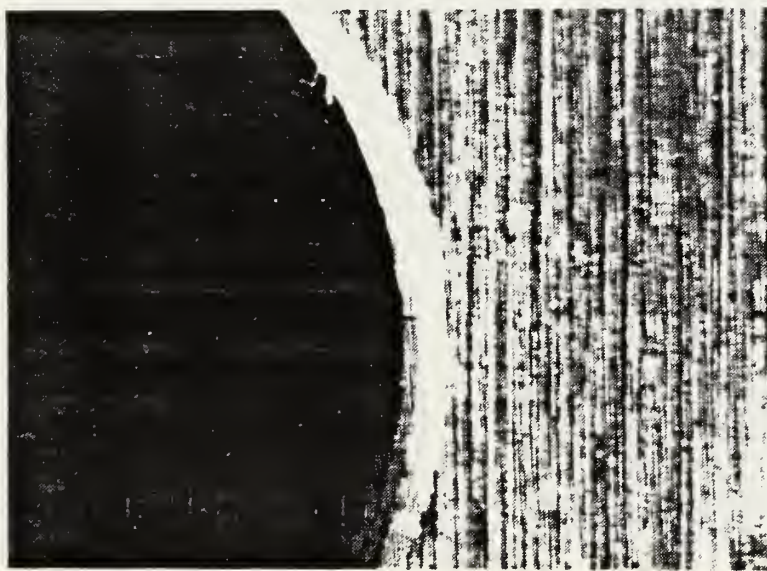
Time 50 μ s/div CHANNEL 3

Figure B.5: Lead break, hole 1, filtered, with cap angles.

APPENDIX C: CRACK/NOISE SIGNALS

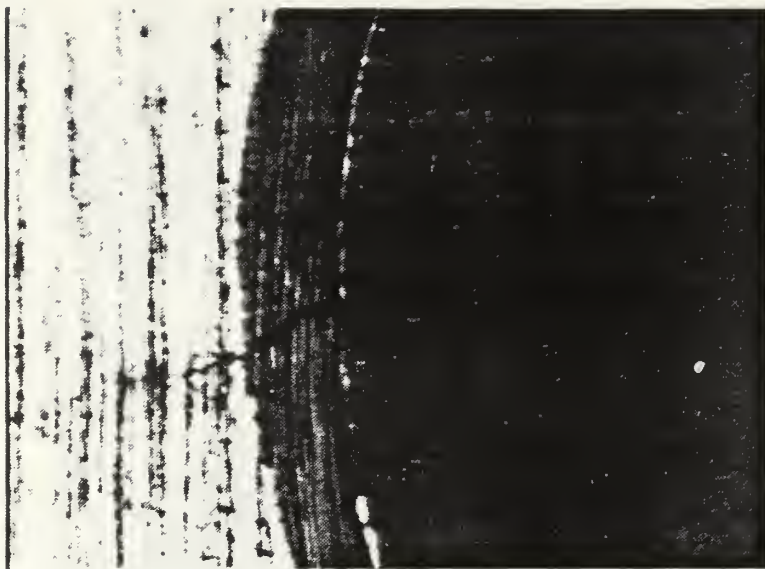


Hole 1, 0.0025" crack, 150x

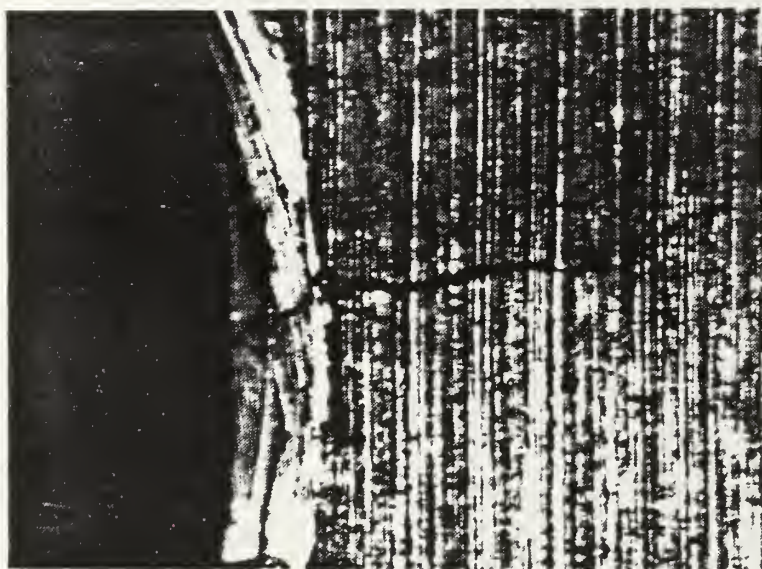


Hole 2, 0.0015" crack, 70x

Figure C.1(a): Test Specimen III cracks

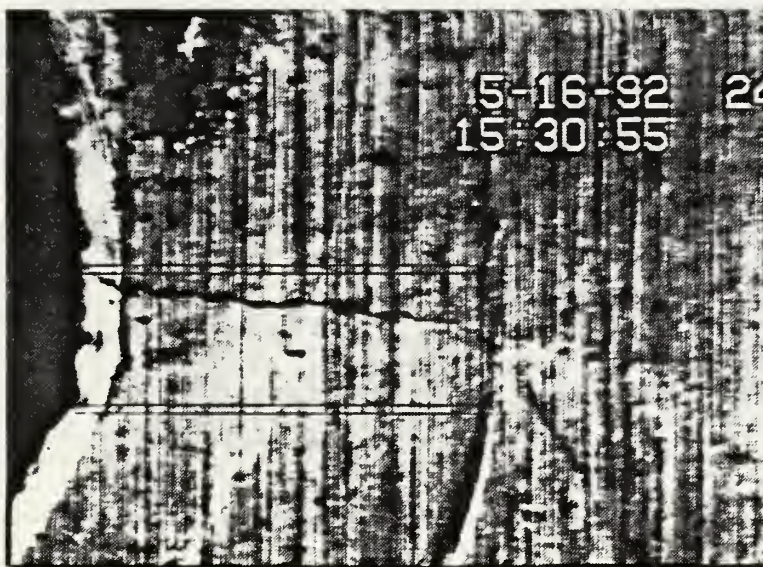


Hole 3, 0.005" crack, 150x



Hole 4, 0.007" crack, 150x

Figure C.1(b): Test Specimen III cracks



Hole 3, 0.028" crack, 70x - Before

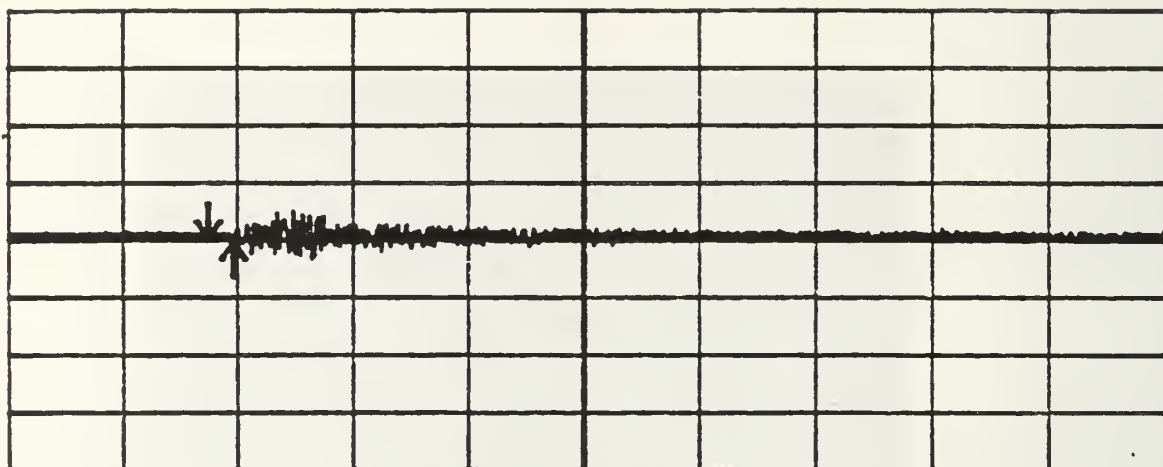


Hole 3, 0.039" crack, 70x - After

Figure C.2: Test Specimen III video sequence

0.4V

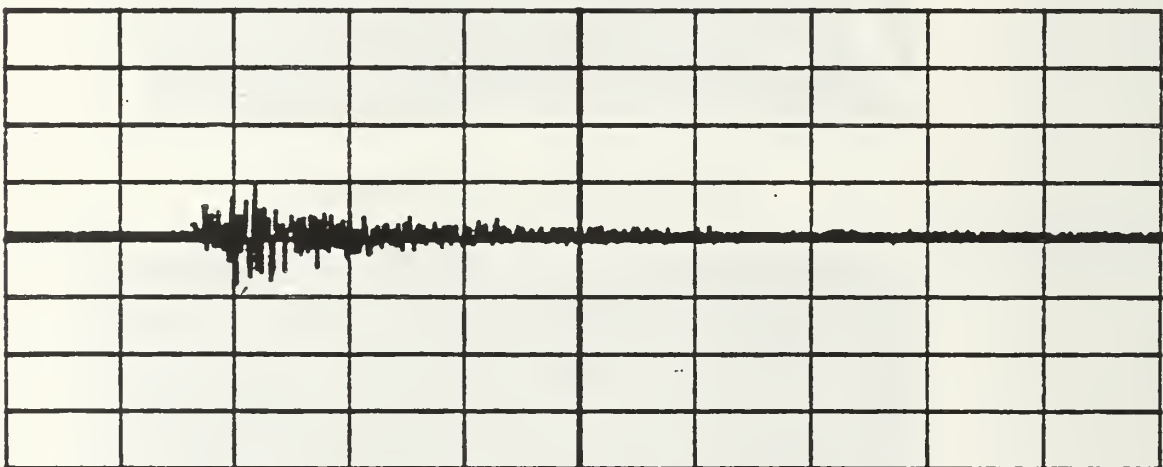
0V



Time 50 μ s/div CHANNEL 1

0.4V

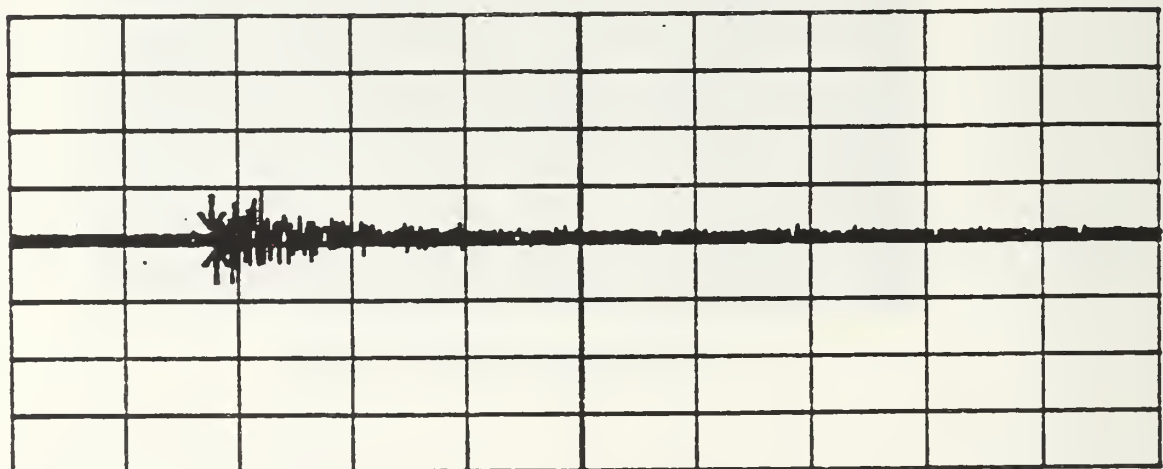
0V



Time 50 μ s/div CHANNEL 2

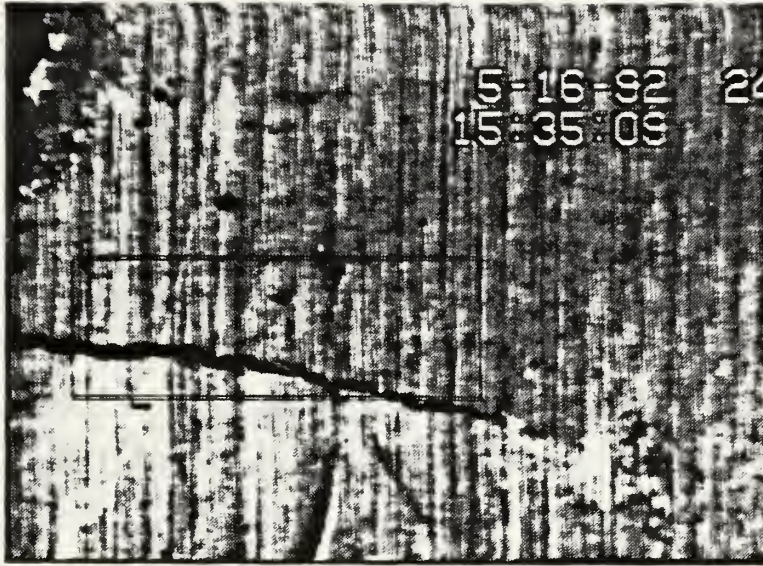
0.4V

0V

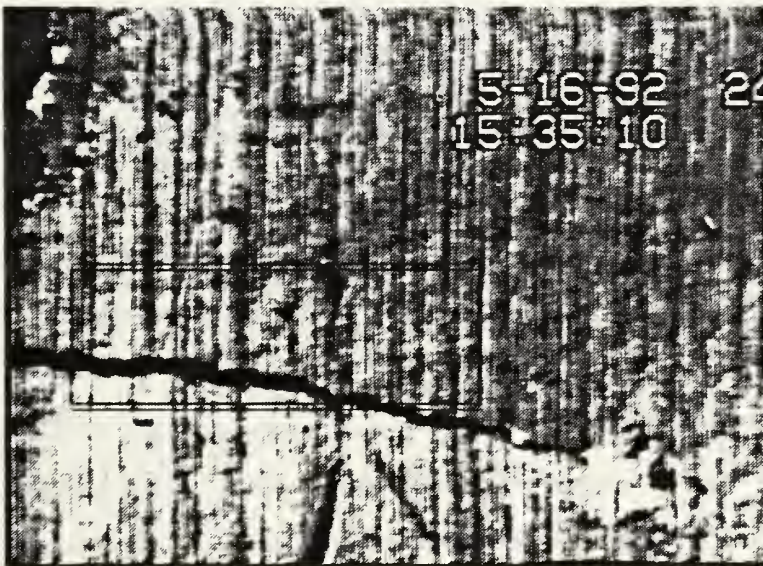


Time 50 μ s/div CHANNEL 3

Figure C.3: Crack hole 3, filtered

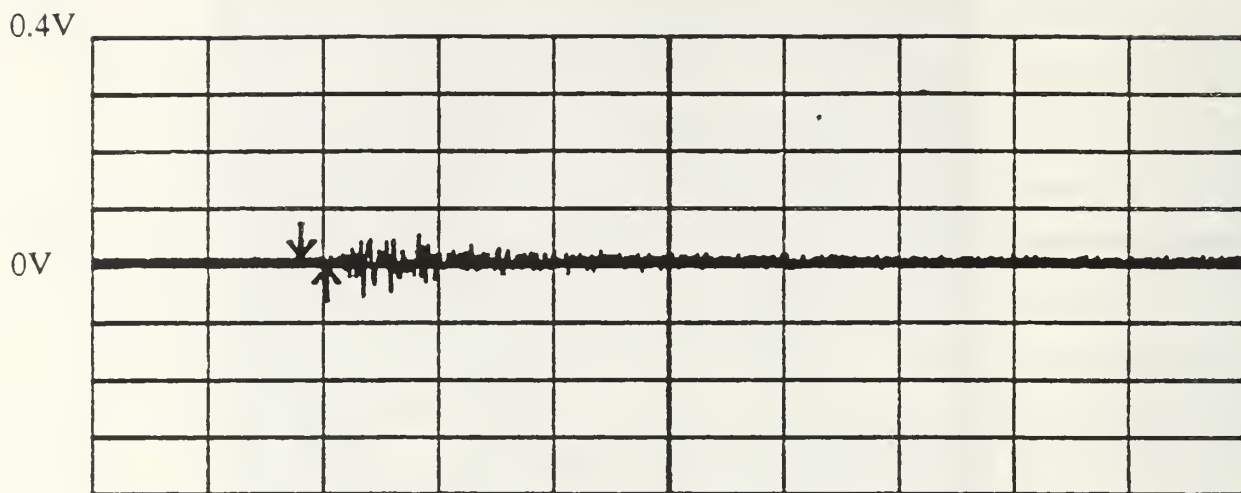


Hole 3, 0.039" crack, 70x - Before

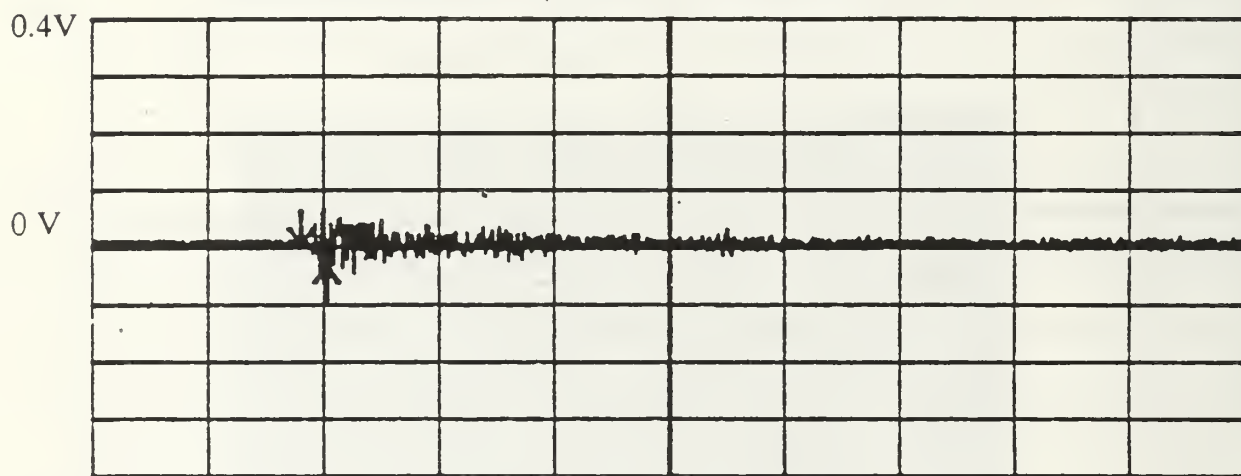


Hole 3, 0.044" crack, 70x - After

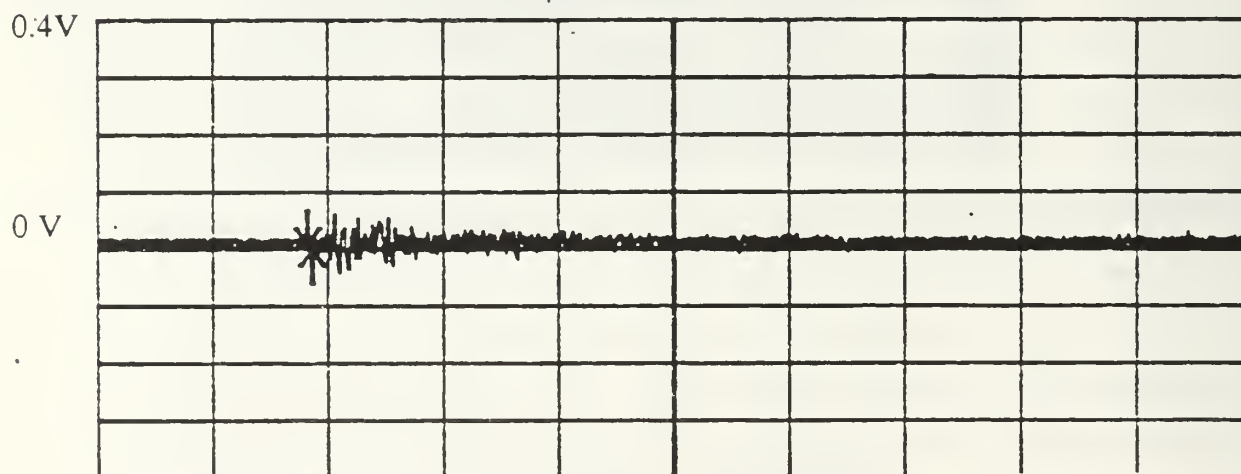
Figure C.4: Test Specimen III video sequence



Time 50µs/div CHANNEL 1

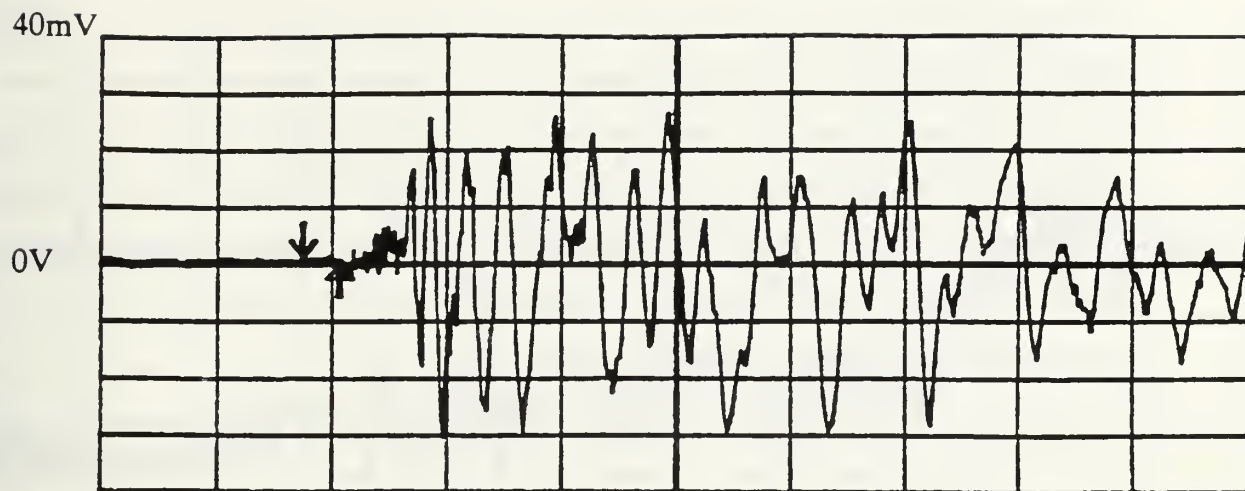


Time 50µs/div CHANNEL 2

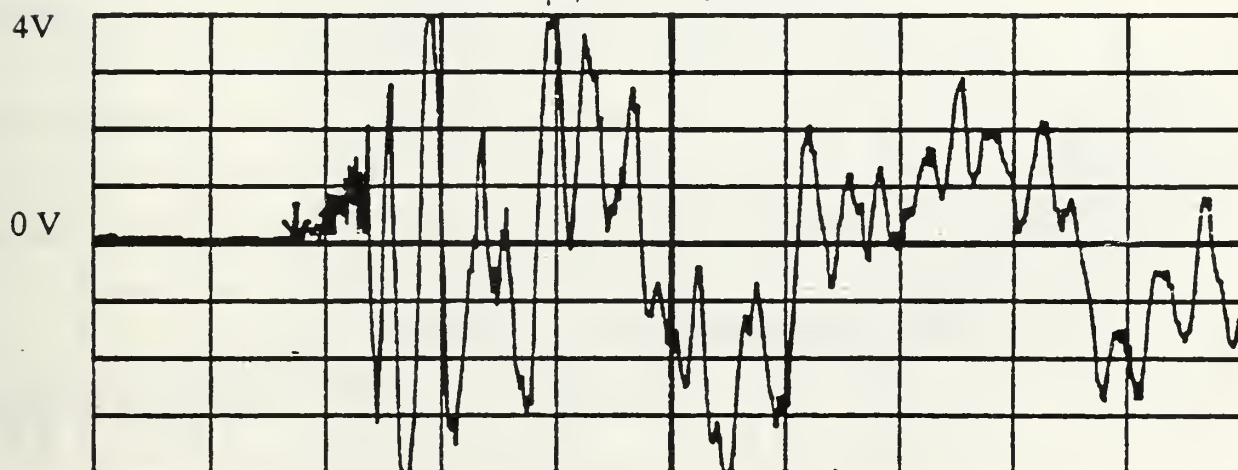


Time 50µs/div CHANNEL 3

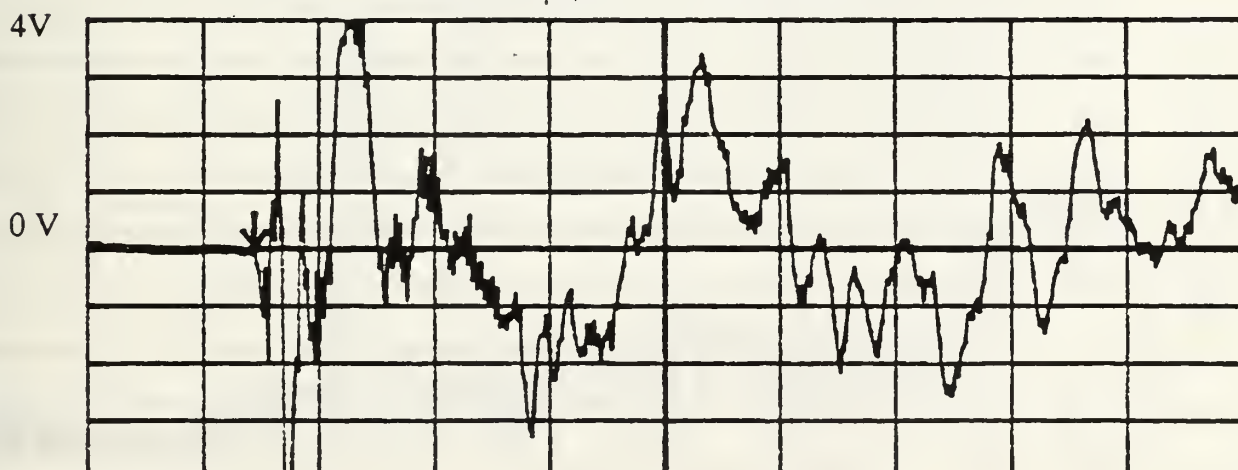
Figure C.5: Crack hole 3, filtered



Time 20 μ s/div CHANNEL 1



Time 20 μ s/div CHANNEL 2



Time 20 μ s/div CHANNEL 3

Figure C.6: Noise, unfiltered, without cap angles.

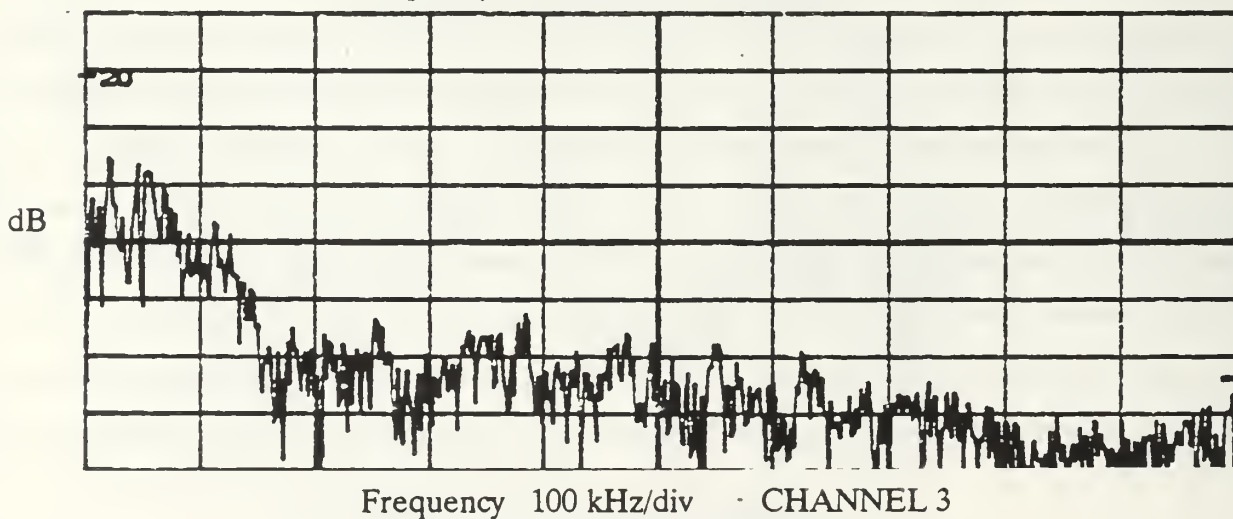
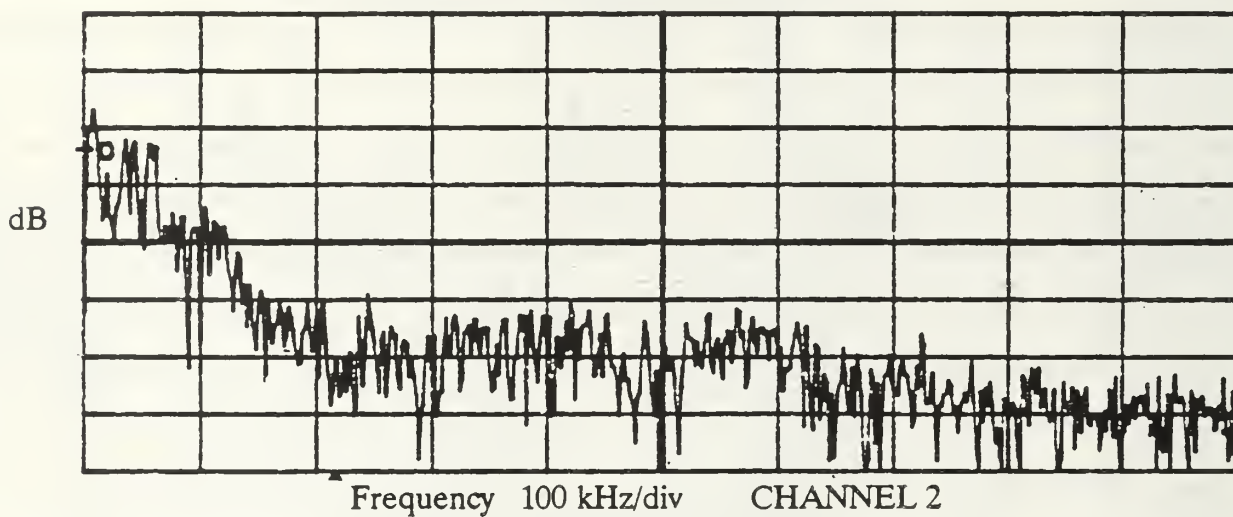
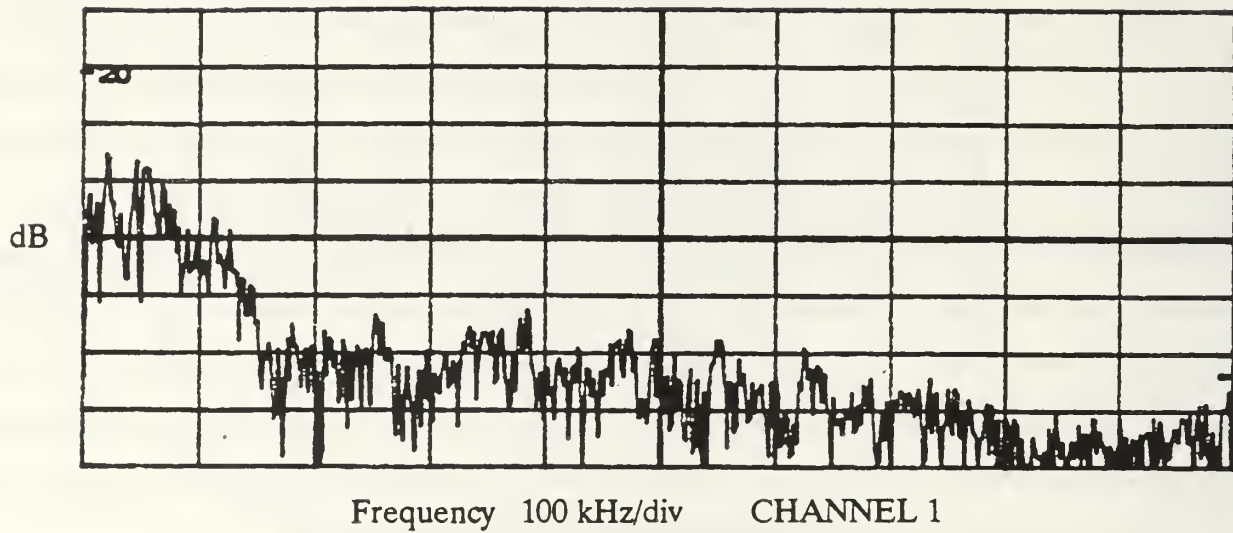
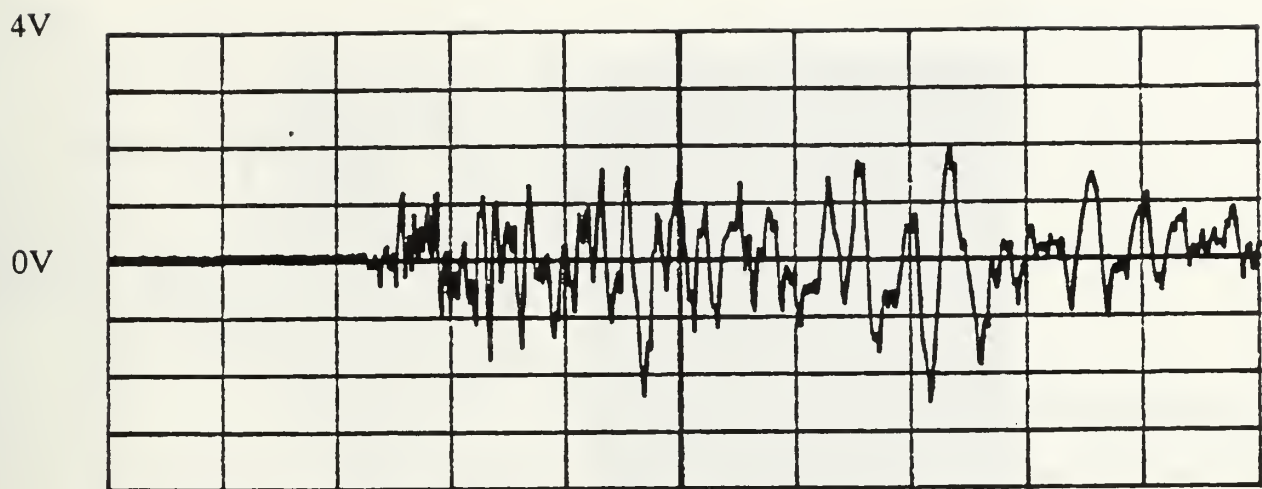
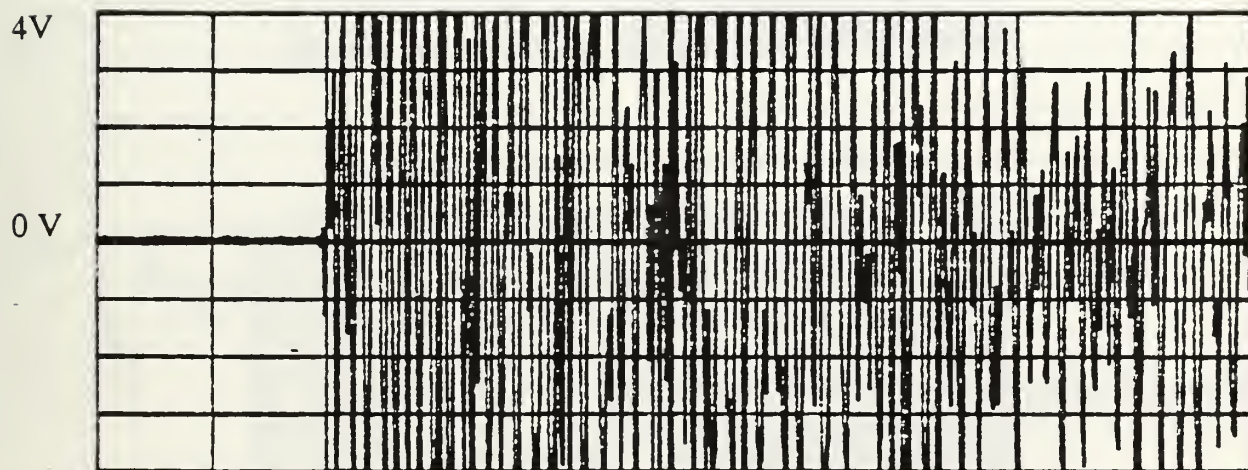


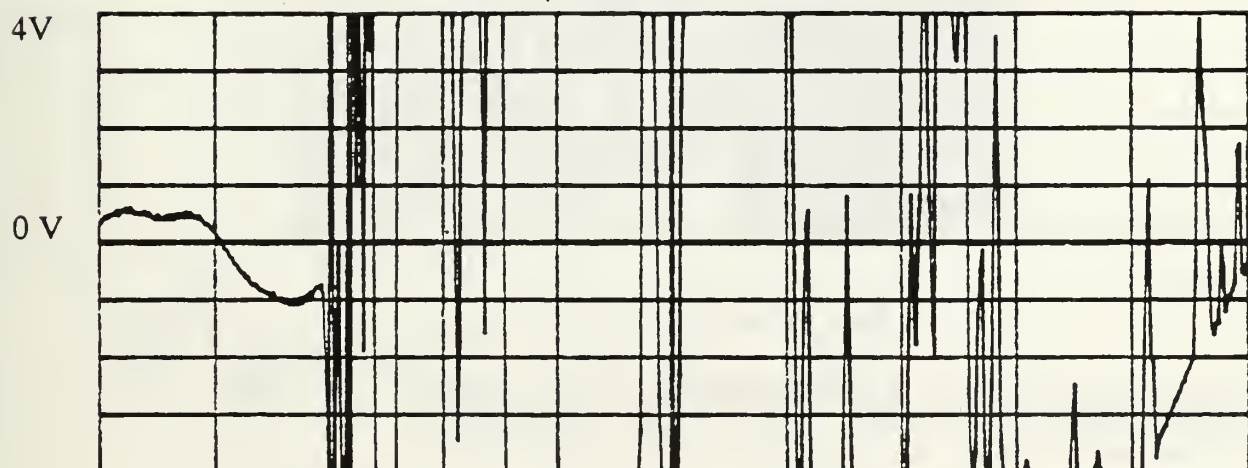
Figure C.7: FFT of Figure 6



Time 50 μ s/div CHANNEL 1

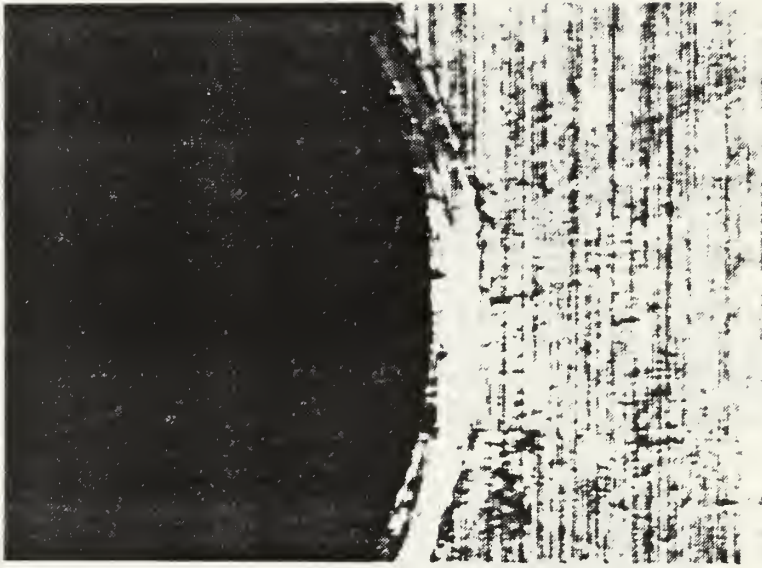


Time 50 μ s/div CHANNEL 2

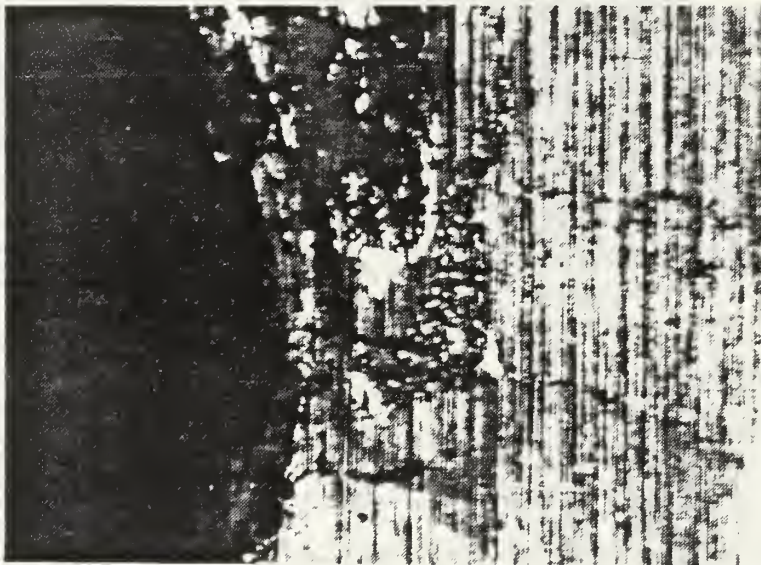


Time 50 μ s/div CHANNEL 3

Figure C.8: Noise, unfiltered, with cap angles.



Hole 1 - Before attachment of cap angles



Hole 1 - After attachment of cap angles

Figure C.9: Cap angle fretting

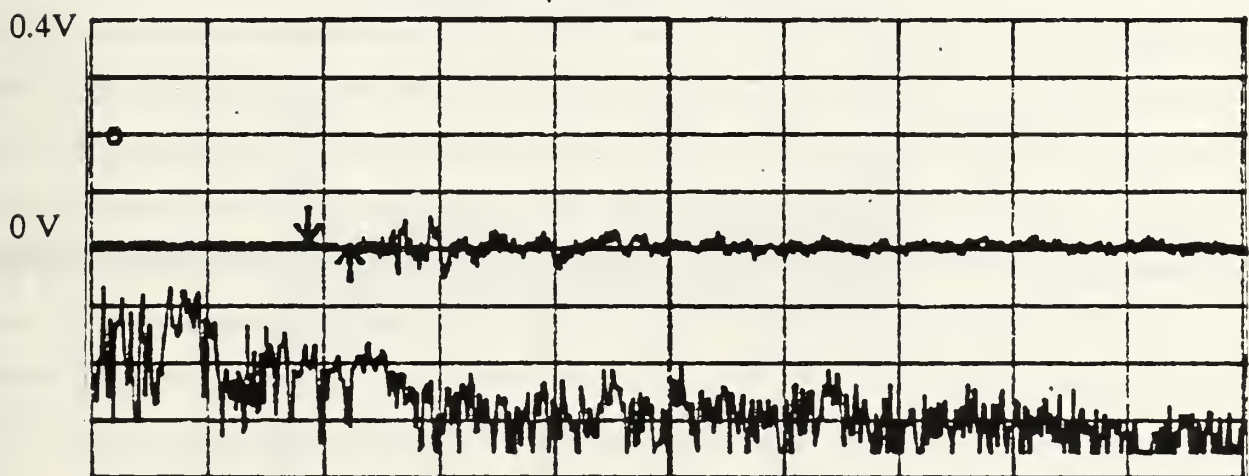
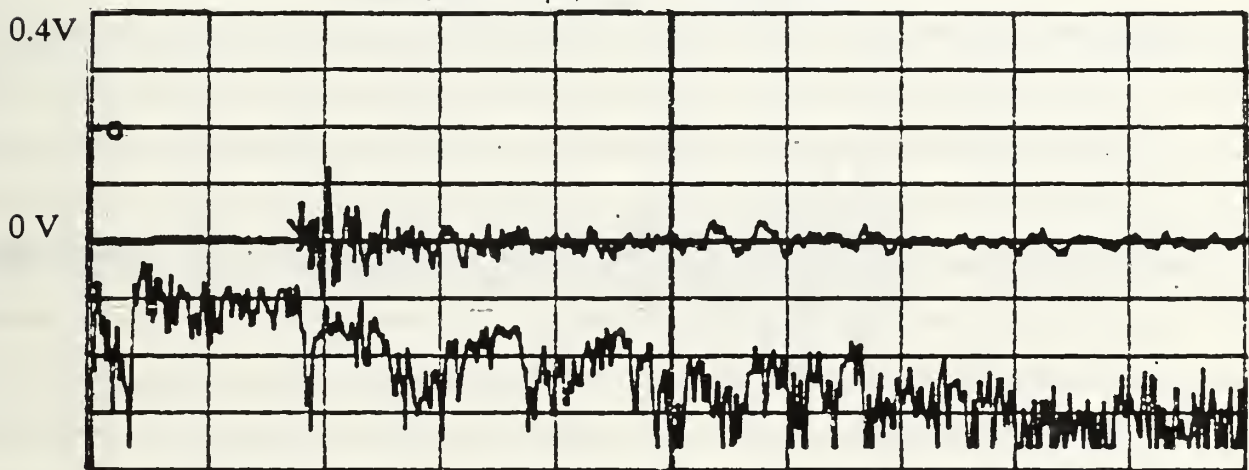
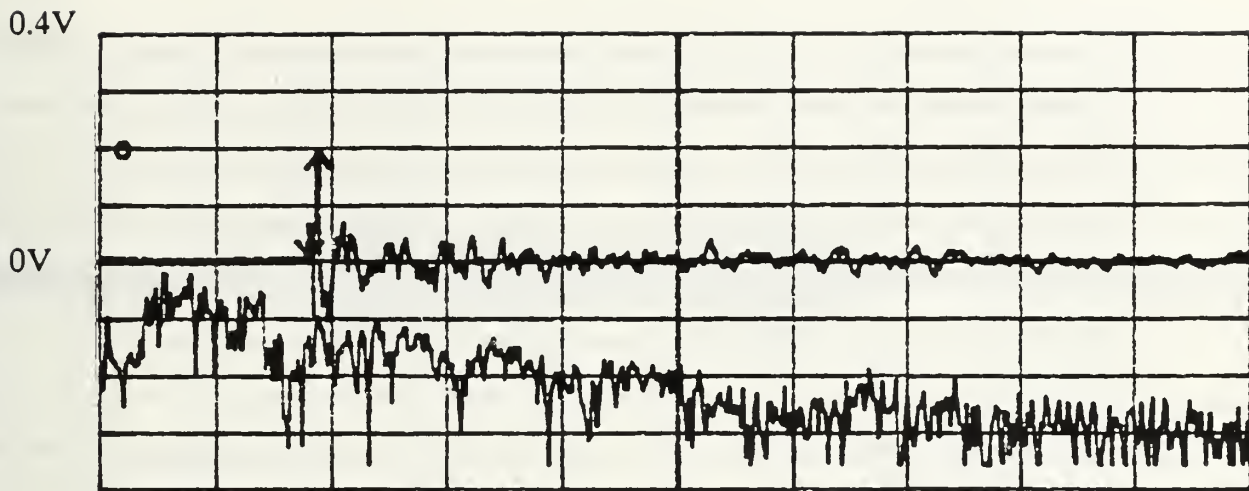
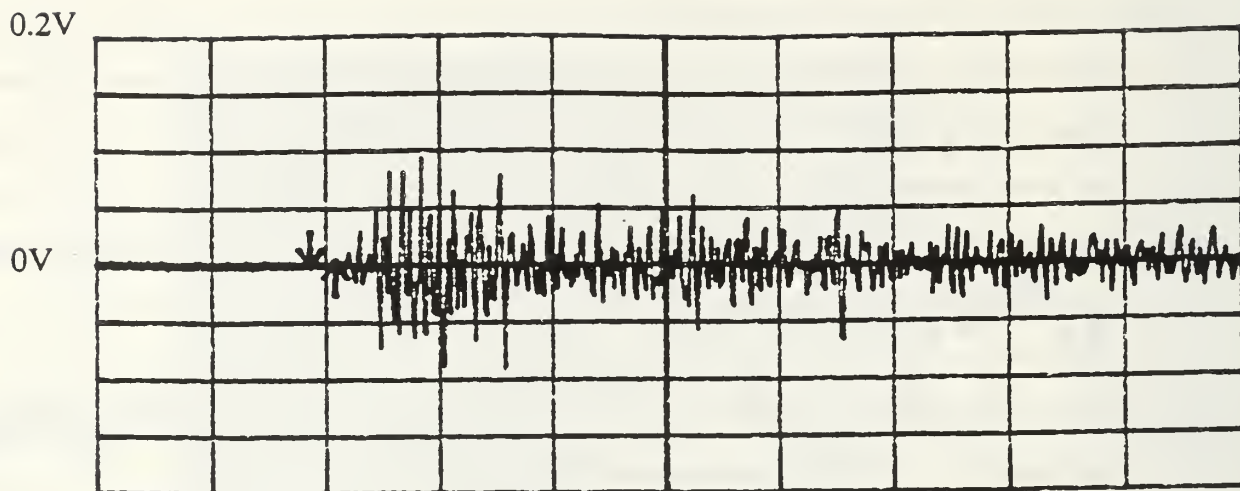
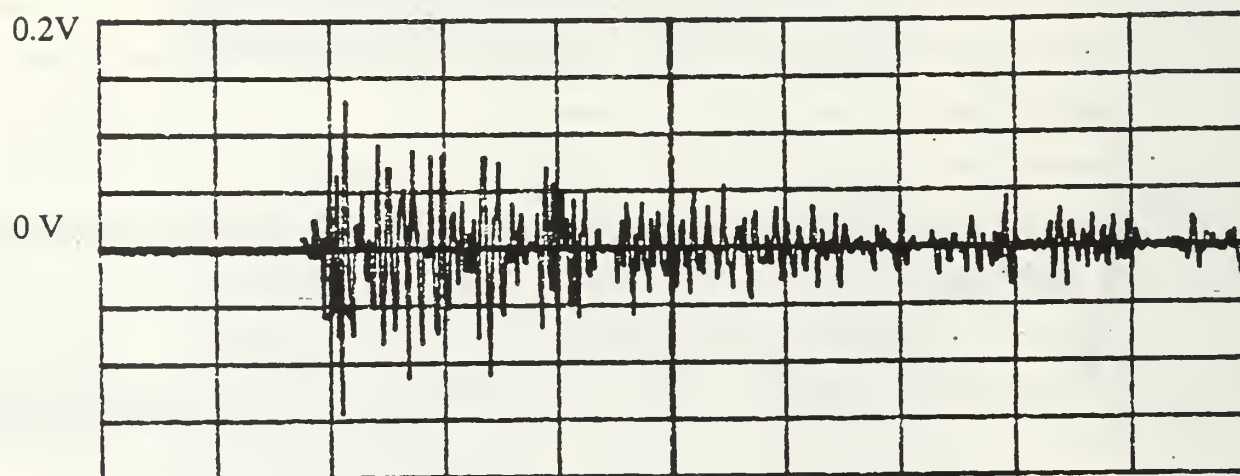


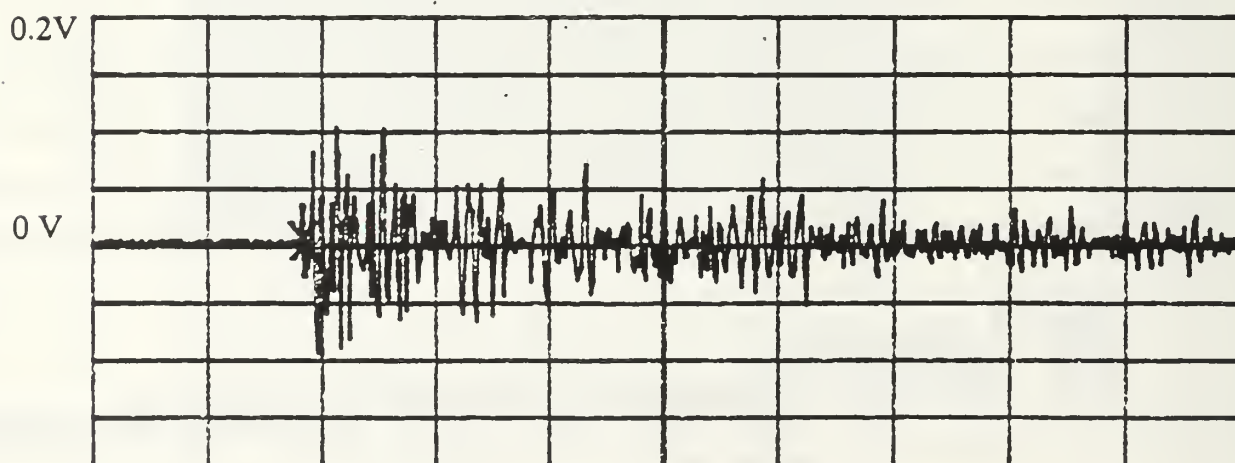
Figure C.10: Crack hole 1,unfiltered, without cap angles.



Time 0.5ms/div CHANNEL 1



Time 0.5ms/div CHANNEL 2

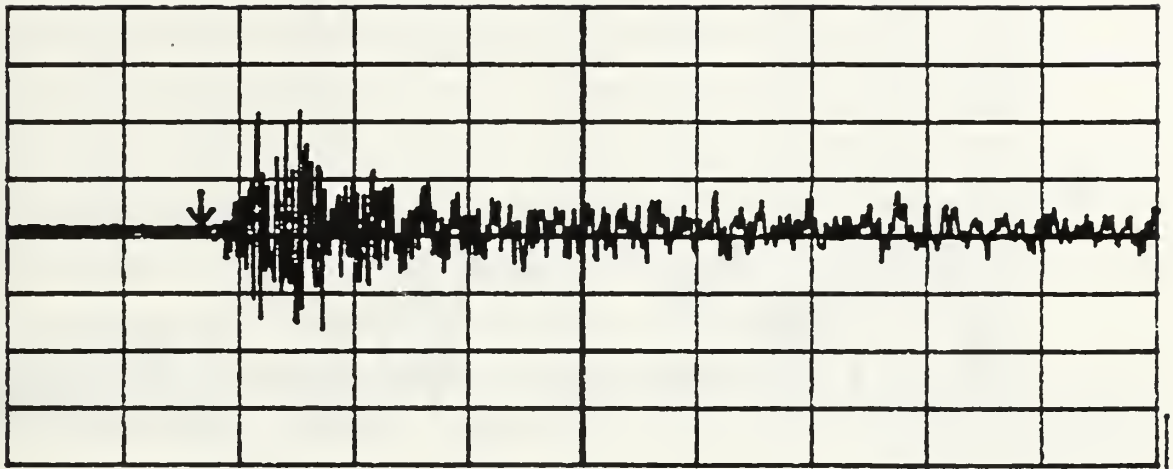


Time 0.5ms/div CHANNEL 3

Figure C.11: Crack hole 3, unfiltered, with cap angles.

40mV

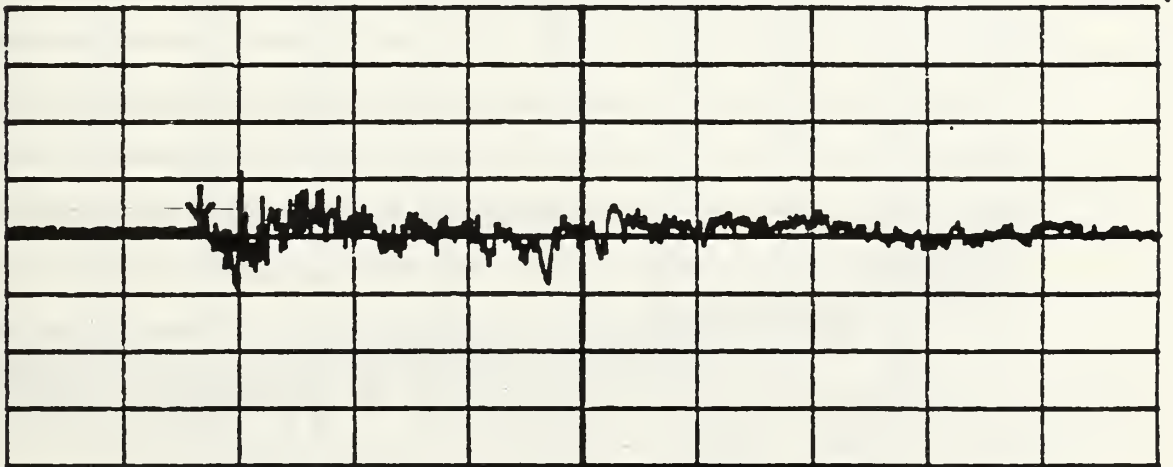
0V



Time 20 μ s/div CHANNEL 1

4V

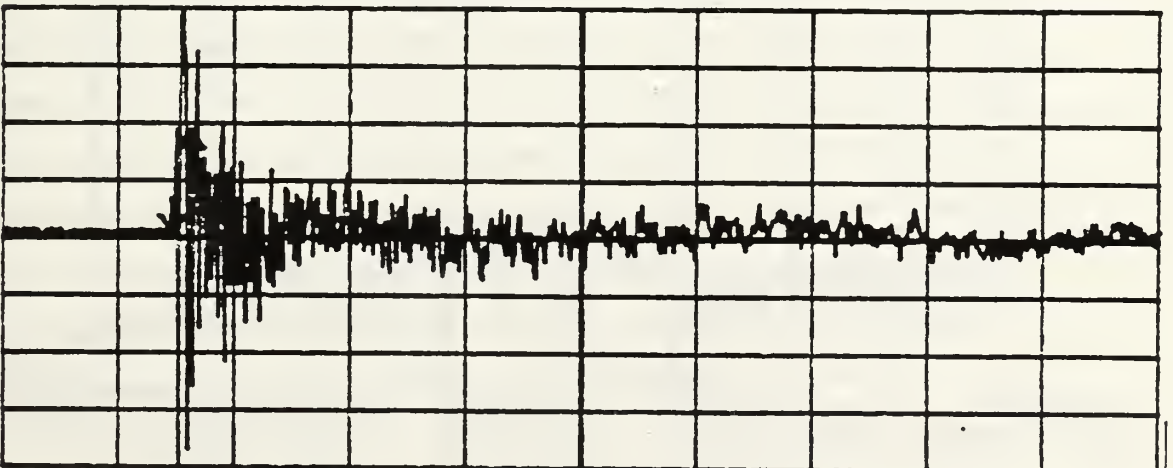
0V



Time 20 μ s/div CHANNEL 2

4V

0V



Time 20 μ s/div CHANNEL 3

Figure C.12: Crack hole 4, unfiltered, with cap angles.

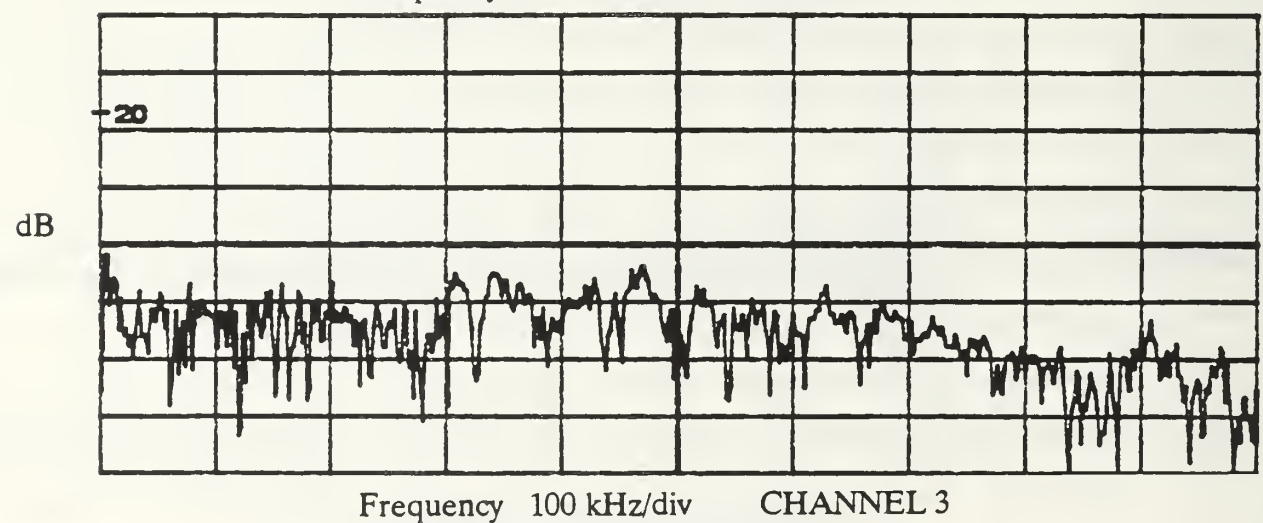
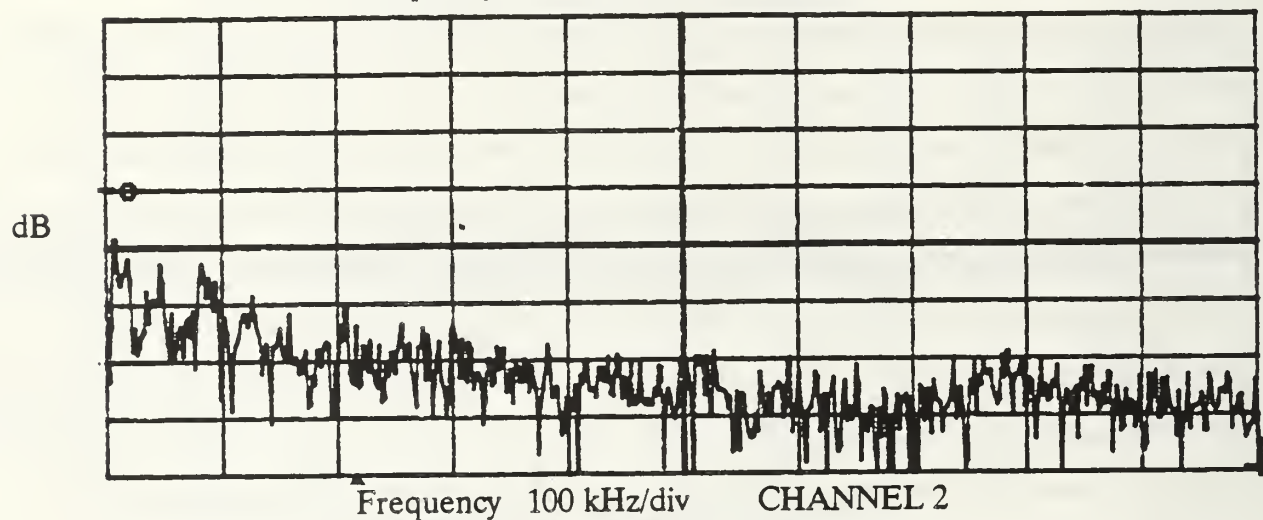
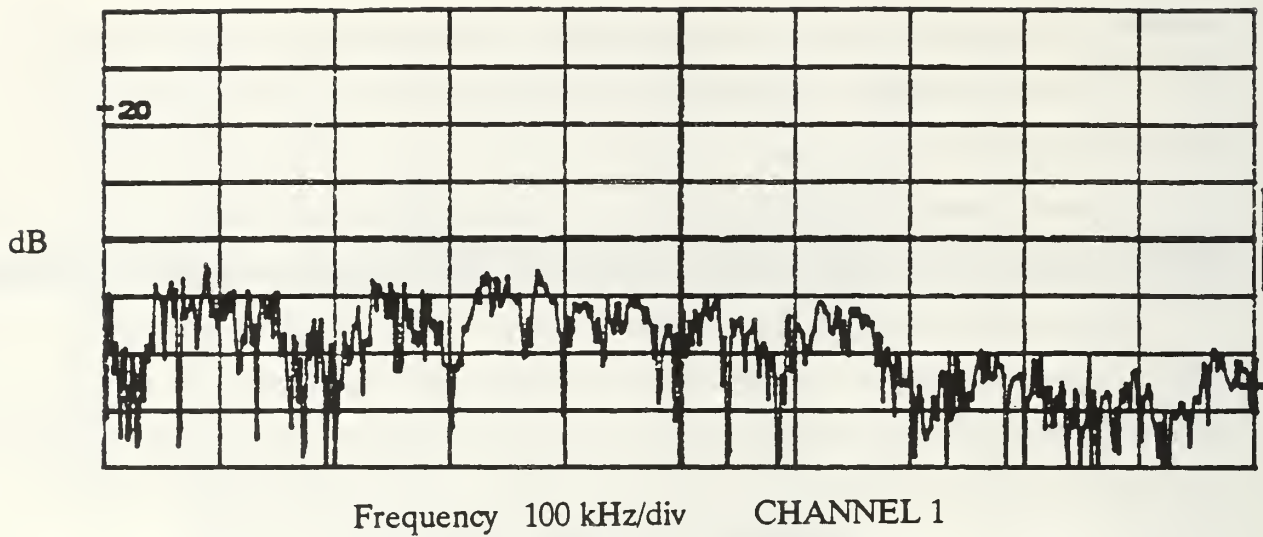


Figure C.13: FFT of Figure 12

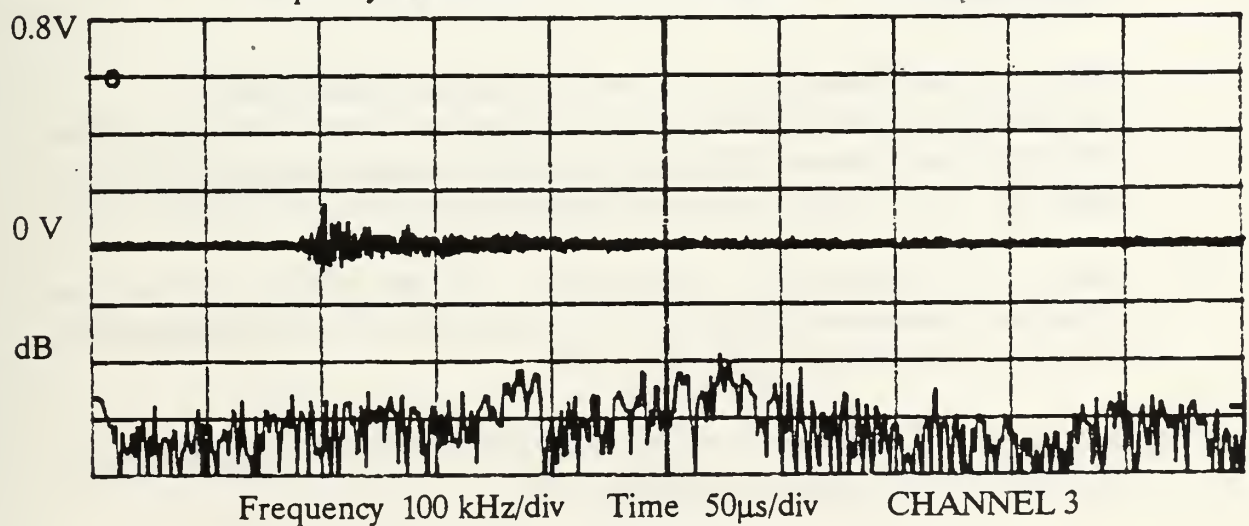
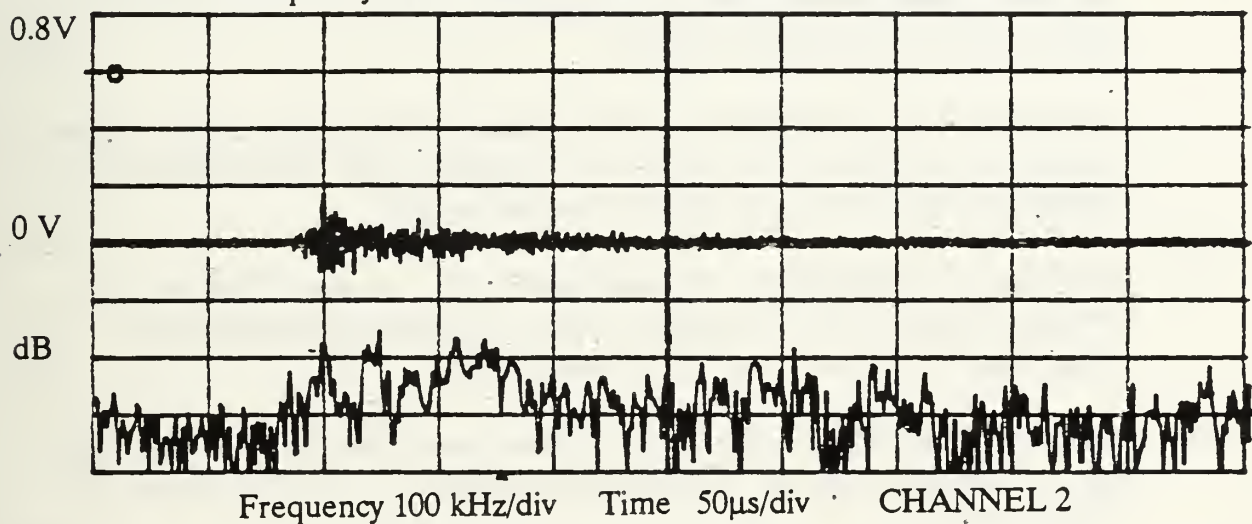
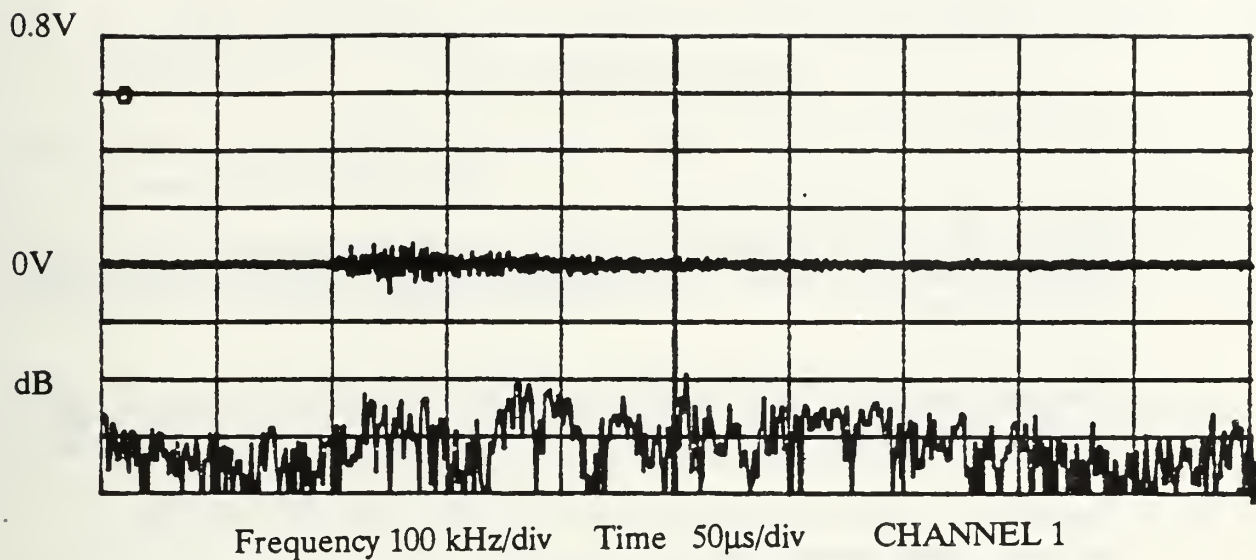


Figure C.14: Crack hole 3, filtered, with cap angles.

LIST OF REFERENCES

1. Smith, W. D., Acoustic Emission from Spectrum Fatigue Cracks in 7075 Aluminum, Master's Thesis, Naval Postgraduate School, Monterey, California, December 1990.
2. Grumman Aerospace Corporation Report 3380.02, Test Plan for Fatigue Test of E-2C Aircraft, by R. Price, S. Campbell and T. Balderes, pg.7, 30 June 1984.
3. Grumman Aerospace Corporation Report AV123-U-RP-292, E-2C Fatigue Test Wing Center Section Teardown Inspection Report, by P. Moll and J. Savalli, pg. 1.0.1, 21 November, 1989.
4. Gerberich, W. W. and Hartblower, C.E., "Some Observations on Stress Wave Emission as a Measure of Crack Growth," International Journal of Fracture Mechanics, Vol. 3, No. 3, pp. 185-191, September 1967..
5. McBride, S.L., MacLachlan, J.W., and Paradis, B.P., "Acoustic Emission and Inclusion Fracture in 7075 Aluminum Alloys," Journal of Nondestructive Evaluation, Vol. 2, No. 1, pp. 35-41, January 1981.
6. Harris, D.O., and Morton, T.M., "Acoustic-emission Detection Techniques for High-cycle-fatigue Testing," Experimental Mechanics, Vol. 13, No. 5, pp. 193-198, May 1973.
7. Wadin, J.R., and Dunegan, H.L., "The Use of Spatial Filtering and Distribution Analysis of Acoustic Emission Signals to Isolate and Characterize Subcritical Crack Growth," The Third Acoustic Emission Symposium, Tokyo, Japan, pp. 183-193, Japan Industrial Planning Association, pp. 183-193, 1976.
8. Bailey, C.D., Hamilton, J.M., and Pless, W.M., "AE Monitoring of Rapid Crack Growth in a Production-size Wing Fatigue Test Article," NDT International, Vol. 9, No. 6, pp. 298-304, December 1976.
9. Gorman, M.R., "Plate Wave Acoustic Emission' submitted to Journal of the Acoustical Emission Society of America, 1990.

10. Graff, K.F., Wave Motion in Elastic Solids, pp. 229-236, Ohio State University Press, 1975.
11. Achenbach, J.D., Wave Propagation in Elastic Solids, pp. 257-258, American Elsevier Publishing Co., 1973.
12. Horowitz, P. and Hill, W., The Art of Electronics, pp. 36-38, 263-266 and pg. 1067, Cambridge University Press, 1989.
13. Hsu, N.N. and Hardy, S.C., "Experiments in Acoustic Emission Waveform Analysis for Characterization of AE Sources, Sensors and Structures," Elastic Waves and Non-Destructive testing of Materials, pp. 86-106, The American Society of Mechanical Engineers, 1978.

INITIAL DISTRIBUTION LIST

- | | | |
|----|--|---|
| 1. | Defense Technical Information Center
Cameron Station
Alexandria, VA 22304-6145 | 2 |
| 2. | Library , Code 52
Naval Postgraduate School
Monterey, CA 93943-5002 | 2 |
| 3. | Commander
Naval Air Systems Command
Attn: E-2C Class Desk
Naval Air Systems Command Headquarters
Washington, D.C. 20361-0002 | 1 |
| 4. | Dr. M. A. Hamstad
Department of Engineering
University of Denver
Denver, CO 80208-0177 | 1 |
| 5. | Dr. William H. Prosser
Mail Code: 231
Langley Research Center
Hampton, VA 23665-5225 | 1 |
| 6. | Dr. George Sandeckyi
WRDC/FIBEC
WAFB, OH 45433-6553 | 1 |
| 7. | Dr. William R. Scott
Code 6063
Naval Air Development Center
Warminster, PA 18974 | 1 |

- | | | |
|----|--|---|
| 8. | Mr. William T. Flatley
A39-06, Grumman Aerospace Corporation
Grumman Blvd
Calverton, NY 11933 | 1 |
| 9. | Dr. Michael R. Gorman
916 E. Phillips Lane
Littleton, CO 80122 | 5 |

DUDLEY KNOX LIBRARY
NAVAL POSTGRADUATE SCHOOL
MONTEREY CA 93943-5101



GAYLORD S



DUDLEY KNOX LIBRARY



3 2768 00018896 5